JOURNAL OF GEOPHYSICAL RESEARCH, VOL. 115, A08213, doi:10.1029/2009JA014663, 2010

Moderate geomagnetic storm (21–22 January 2005) triggered by an outstanding coronal mass ejection viewed via energetic neutral atoms

Susan McKenna-Lawlor,[1] Lu Li,[2] Iannis Dandouras,[3] Pontus C. Brandt,[4] Yihua Zheng,[4]
Stas Barabash,[5] Radoslav Bucik,[6] Karel Kudela,[7] Jan Balaz,[1,7] and Igor Strharsky[1,7]

Received 21 July 2009; revised 19 October 2009; accepted 5 November 2009; published 14 August 2010.

[1] An outstanding flare on 20 January 2005 was accompanied by a coronal mass ejection which arrived at the magnetopause at ~1712 UT, 21 January, and produced a strong compression-pressure pulse. Enhanced magnetospheric activity was stimulated. The associated development between <1800 UT and >02.19 UT on 21–22 January, 2005 of a ring current disturbance in energetic neutral atom (ENA) data, recorded aboard both the Double Star and the IMAGE (Imager for Magnetopause-to-Aurora Global Exploration) spacecraft, is described. A magnetic storm from ~1712 UT, 21 January, reached minimum *Dst* = ~−101 nT at ~0600 UT, 22 January, and its recovery phase endured until 27 January. ENA data indicate that the ring current experienced a deep injection of H^+ and O^+ ions at ~1830 UT when IMF Bz was oriented southward. At this time, the ring current was strongly asymmetric, although later it became more symmetric. Bz turned northward at 1946 UT. From ~0224 to ~0612 UT on 22 January, Bz fluctuated such that it intermittently pointed southward (±10 nT). The moderate but extended response of the geomagnetosphere to the strong pressure pulse is explained by a slow evolution in the orientation of Bz under conditions of enhanced plasma sheet density. Modeling of dynamical parameters that represent various current systems that contributed to *Dst* revealed their individual characteristics. The changing geomagnetic field was also modeled. Comparisons with ENA data show that early asymmetric enhancements recorded in hydrogen and oxygen were accompanied by intensified external current systems that produced a magnetic field related compression of the magnetosphere. The gradual reduction in ring current asymmetry was complemented by the largely symmetrical configuration displayed by the corresponding, still intensified, modeled magnetic field.

Citation: McKenna-Lawlor, S., L. Li, I. Dandouras, P. C. Brandt, Y. Zheng, S. Barabash, R. Bucik, K. Kudela, J. Balaz, and I. Strharsky (2010), Moderate geomagnetic storm (21–22 January 2005) triggered by an outstanding coronal mass ejection viewed via energetic neutral atoms, *J. Geophys. Res.*, *115*, A08213, doi:10.1029/2009JA014663.

1. Introduction

1.1. Solar Activity in January 2005

[2] An outstanding solar flare (Class X-7.1) on 20 January 2005 at solar coordinates N14, W61 (Active Region AR 0729) stimulated the largest ground level event (GLE) produced at the Earth in 50 years [*Belov et al.*, 2005; *Bieber et al.*, 2005; *Flückiger et al.*, 2005; *Ryan et al.*, 2005]. This flare came at the end of a sequence of significant soft X-ray events recorded in the same active region by GOES 10 and CORONAS-F. *Paxton et al.* [2005] reported that flare associated energetic particles filled both polar caps for ~10 days in association with the complex activity of January 2005.

[3] The spectra of particles associated with the flare [e.g., *Mewaldt et al.*, 2005; *Krucker et al.*, 2005; *Kuznetsov et al.*, 2005, 2006a, 2006b; *Share et al.*, 2006] indicated the presence of ions accelerated up to at least 200–300 MeV. These spectra were among the hardest ever recorded. Signatures of ground level events marking the associated arrival at Earth of particles with energies up to 20–30 GeV are described in a plethora of papers that include those by *Bieber et al.* [2005], *D'Andrea and Poirier* [2005],

---

[1] Space Technology Ireland, National University of Ireland, Maynooth, Ireland.

[2] Center for Space Science and Applied Research of the Chinese Academy of Sciences, Beijing, China.

[3] Centre d'Etude Spatiale des Rayonnements, Université de Toulouse, and UMR 5187, CNRS, Toulouse, France.

[4] Johns Hopkins University Applied Physics Laboratory, Laurel, Maryland, USA.

[5] Swedish Institute of Space Physics, Kiruna, Sweden.

[6] Max Planck Institute for Solar System Research, Lindau, Germany.

[7] Institute of Experimental Physics, Kosice, Slovakia.

0148-0227/10/2009JA014663

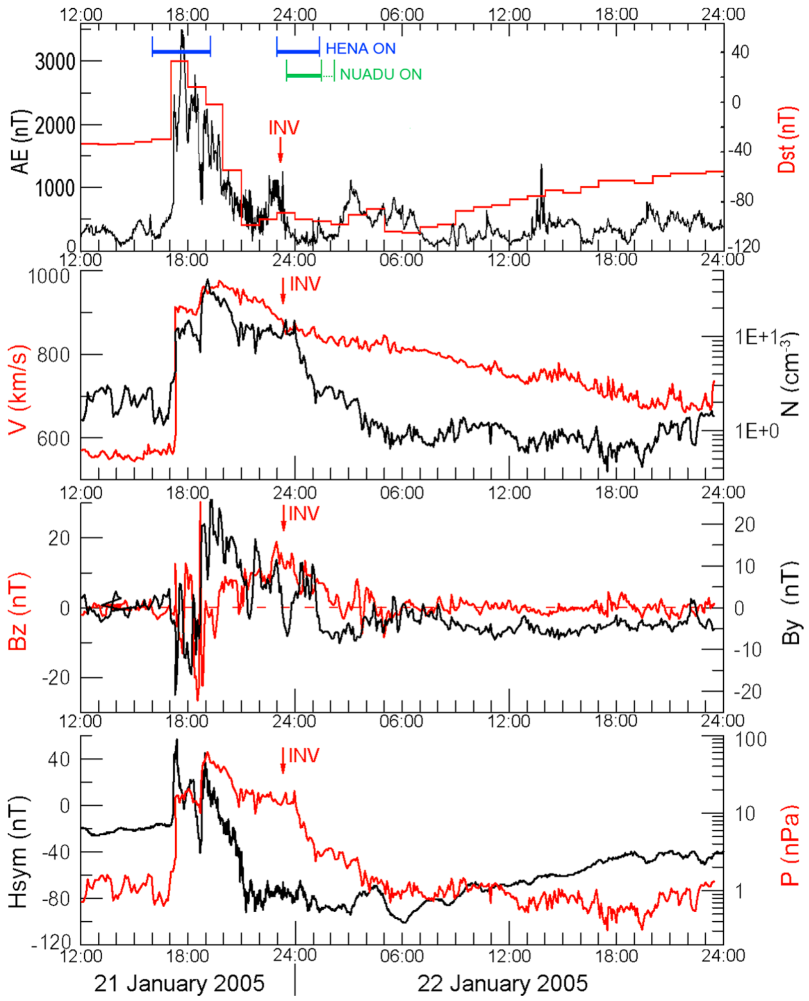

Figure 1. Interplanetary plasma and magnetic field data from 12.00 UT on 21 January to 24.00 UT on 22 January, 2005. The individual plots show: first panel, the *AE* Index (black) and the *Dst* Index (red); second panel, the solar wind density (black) and the solar wind velocity (red) at 1 AU; third panel, the magnetic field components By (black) and Bz (red); fourth panel, the dynamic pressure P (black) and SYM-H (red). These data plots are based on information kindly provided by K. Kalegaev (private communication, 2006) [see also *Kalegaev*, 2006]. The times when High-Energy Neutral Atom (HENA) and Neutral Atom Detector Unit (NUADU) observations were made are indicated by heavy blue and green lines, respectively. A period between 0130 and 0219 UT on 22 January, when NUADU observations were made but contaminated by light, is indicated by a light green line. The arrow (INV) indicates a time at which ion distributions retrieved from simultaneous NUADU and HENA data were compared (Figure 9).

Miyasaka et al. [2005], *Ryan et al.* [2005], and *Bastanjyan et al.* [2007].

1.2. Geomagnetic Activity in January 2005

[4] Three magnetic storms associated with successive flares in active region HAO-AR 0729 occurred during January 2005. The first started at ~1400 UT on 7 January, reached minimum $Dst = -105$ nT at 0300 UT on 8 January and its recovery phase continued until 11 January. The second started at ~2200 UT on 16 January and reached minimum $Dst = -125$ nT at 0900 UT on 18 January.

[5] On 20 January 2005 the Class X 7.1 flare referred to in section 1.1 commenced at 0636 UT. This event was associated with the release of a fast (~2100 km/s), full halo, coronal mass ejection that was imaged from L1 by the LASCO and EIT instruments [*Domingo et al.*, 1995] aboard the SOHO spacecraft. *Foullon et al.* [2007] used multi-spacecraft data (from ACE, Cluster, WIND and Geotail) to derive a picture of the geometry of the ejected solar material which they deduced was composed of nested magnetic loops connected to the Sun.

[6] Figure 1 (first panel) shows (from 1200 UT on 21 January to 2400 UT on 22 January) variations in the *AE* index. Excursions of this index from its nominal, daily baseline are referred to as magnetospheric substorms [*Davis and Sugiura*, 1966], and such events typically display durations ranging from tens of minutes to several hours. Also plotted in the first panel of Figure 1 is the *Dst* index. Minimum $Dst = \sim -101$ nT was reached on 22 January at ~0600 UT. Thereafter, the recovery phase was gradual and

endured until 27 January [*Kuznetsov et al.*, 2006b]. This low-level, long-lived disturbance was initiated while the magnetosphere was already disturbed owing to its responses to preceding activity in the same solar region. It is noted that the maximum *Kp* index attained was 8 and that this extended over only a single 3 h interval.

[7] The second panel of Figure 1 shows contemporary increases in the speed and density of the solar wind, and the third panel shows ongoing changes in Bz and By. Since *Wanliss and Showalter* [2006] pointed out that SYM-H can be used as a de facto, high-resolution *Dst* index, high time resolution (1 min) variations in SYM-H are displayed in the fourth panel. Also plotted is the solar wind pressure. Since extremely high solar wind pressure that might have influenced the SYM-H measurements pertained on 21 January, pressure corrected variations SYM-H* were calculated from SYM-H by *Du et al.* [2008] for this event. However, these authors found that, while there were some differences between SYM-H and SYM-H* the main phase growth was initiated at 1946 UT, 21 January in both traces and, thus, the corrected values are not presented here.

[8] A strong interplanetary shock (magnetosonic Mach number 5.4) recorded aboard ACE (then located at X_{GSE} ~ 223 R_E and Y_{GSE} ~ −35.5 R_E) at ~1648 UT produced an SI^+/SSC (Sudden Impulse/Storm Sudden Commencement) which reached −57 nT at ~1712 UT at Earth. The fast ICME caused significant compression of the magnetosphere, and *Dandouras et al.* [2008] reported that the resulting standoff distance from the subsolar point was $X = 4.5\ R_E$. There is evidence also of the occurrence of a large Forbush effect in association with the shock related compression [*Yanke et al.*, 2005]. The enhanced southward IMF Bz present in the sheath following the shock produced a decrease in SYM-H to ~ −41 nT.

[9] At the time of the large pressure pulse the Cluster and Double Star Earth orbiting constellations were both located in the afternoon sector. Cluster, which was in the solar wind, recorded an approximately fourfold increase in proton density at about 1710 UT (Cluster Ion Spectrometry/CIS data). Also the solar wind velocity (V_{sw}) increased from ~560 to 900 km^{-1} across the shock. The Double Star (TC-1) spacecraft, which was then following an inbound trajectory within the magnetosheath, unexpectedly transited the bow shock at 1853 UT owing to the sudden compression. Thereafter, it remained in the solar wind for some 14 min before reentering the magnetosheath at $R < 8.5\ R_E$ [*Vallat et al.*, 2005; *Dandouras et al.*, 2009].

[10] A double discontinuity, characterized by a non-compressive density enhancement (NCDE) was recorded aboard ACE at 1823 UT and reached Earth at 1843 UT where it stimulated a second SI^+/SSC (~−25 nT) at ~1847 UT. The first discontinuity had a normal angle of 83° while the second had a normal angle of 74° relative to the IMF. This pair of features constituted nearly parallel tangential discontinuities. However, only a single discontinuity was detected in the solar wind density and temperature parameters [*Du et al.*, 2008]. When at 1946 UT the IMF Bz turned northward the main phase of the storm began. Between ~0600 and 0700 UT a minimum value of *Dst* = ~101 nT was attained. The recovery phase took place thereafter. It is especially noted that, in contrast to the many significant signatures reported to occur in the terrestrial environment in response to the major flare of 20 January, the geomagnetic storm of 21 January was a rather minor event.

1.3. Present Study

[11] An investigation is made in the present study of the ring current recorded in energetic neutral atom (ENA) data during 21 and 22 January 2005. These measurements were made from different vantage points by the High-Energy Neutral Atom (HENA) instrument aboard the Imager for Magnetopause-to-Aurora Global Exploration (IMAGE) spacecraft and by the NeUtral Atom Detector Unit (NUADU) instrument aboard the Double Star–Polar (TC-2) spacecraft. Accounts of the Double Star and IMAGE missions are contained in the work of *Liu et al.* [2005] and *Burch* [2000], respectively. HENA made observations outside the radiation belts from 1600–1900 UT, 21 January, and from 2300 UT to ~0130 UT, 21–22 January. NUADU observations were made from 2330 UT to 0219 UT, 21–22 January. The observations made after 0130 UT on 22 January were, however, recorded at an unfavorable location (section 2.4) and cannot be analyzed in detail although it is possible to discern in these images that the ring current was disturbed up to at least 0219 UT.

[12] Overall, useful ENA measurements commenced 1 h before the arrival at Earth at ~1712 UT, 21 January of the fast (~2100 km/s) ICME mentioned in section 1.2 (i.e., when the ring current was still quiet). These observations terminated approximately 4.5 h before minimum, negative *Dst* (at ~0600 UT, 22 January).

[13] NUADU (aboard TC-2) and HENA (aboard IMAGE) were, at the time of the major solar related disturbance of 21–22 January, viewing the ring current from different viewpoints. ENA images of a given region of a ring current acquired simultaneously from separate vantage points can potentially provide different pitch angle information concerning the parent ion population. However, extraction of this kind of information was not feasible in the present study. This was because NUADU observed the ring current population from “above” (i.e., from the Northern Hemisphere) at a location very close to the Z_{GSM} axis while HENA observed the ring current population from “below” (i.e., from the Southern Hemisphere) also very close to the Z_{GSM} axis (Figure 2). This was not an appropriate configuration for stereo imaging since the extraction of pitch angle information is best achieved when the two vantage points concerned have a substantial angular separation and also are not at symmetric latitudes from the equator.

[14] Section 2 contains a general account of ENA production and of the instruments (NUADU and HENA) whereby the ENAs considered here were detected. Section 3 presents the ENA data recorded during the geomagnetic storm of 21–22 January and also an account and discussion of both these kinds of observations. Section 4 provides an overview of classical methodologies used to retrieve ion distributions from ENA images. An account of a method recently developed [*Lu et al.*, 2008] to retrieve ion distributions from data measured by NUADU under disturbed geomagnetic conditions is outlined in section 4.2 and described in detail in Appendices A and B. This method is used to derive ion distributions in the ring current recorded by NUADU between 2330 and 2400 UT, 21 January, 0030–0100 UT, 22 January, and 0100–0130 UT, 22 January 2005.

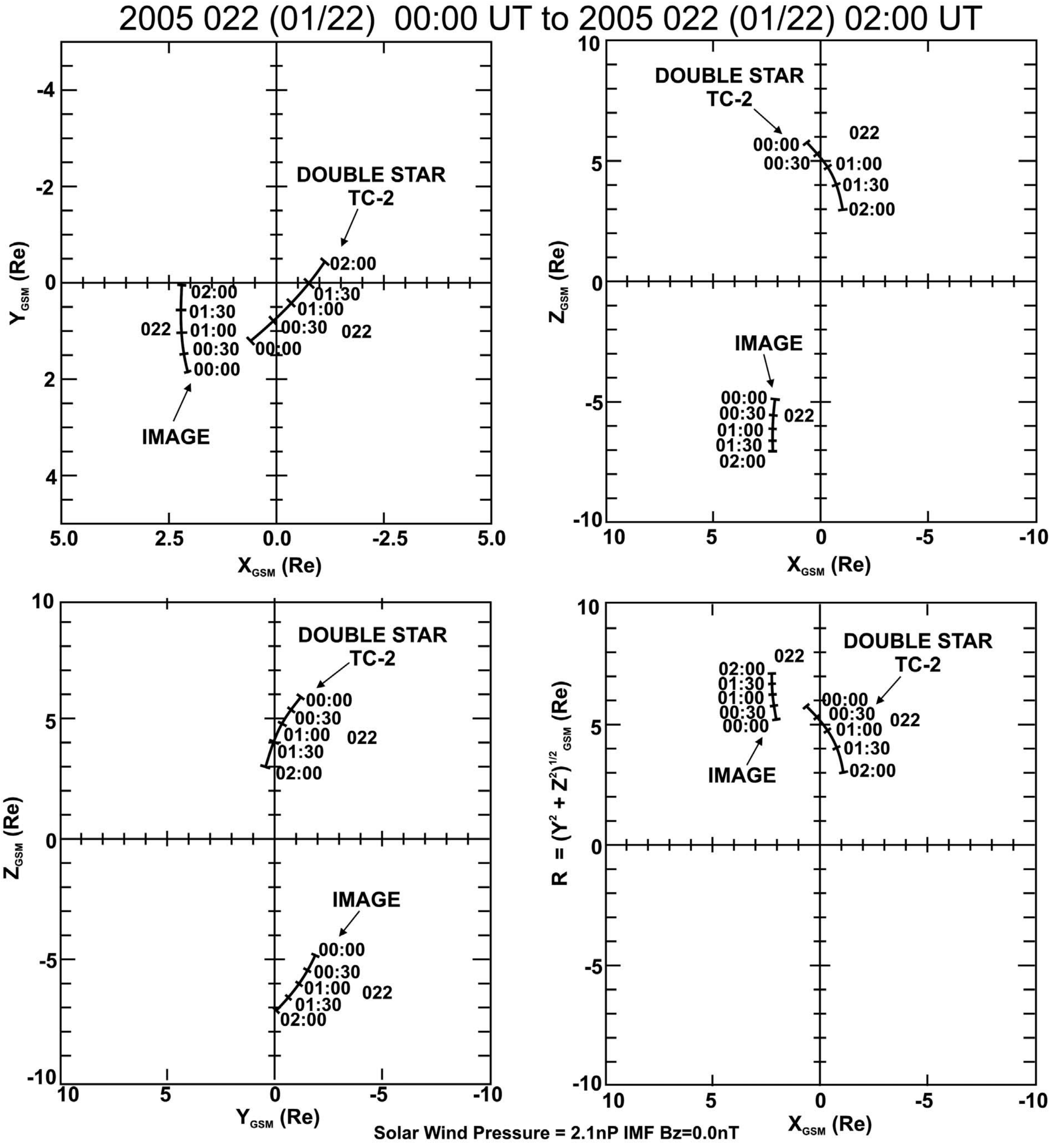

Figure 2. Representative positions in GSM coordinates of the Double Star–Polar (TC-2) and Imager for Magnetopause-to-Aurora Global Exploration (IMAGE) spacecraft on 22 January 2005.

In situ ion measurements made by the RAPID instrument [*Wilken et al.*, 1997] aboard the CLUSTER spacecraft from 2000–2300 UT, 22 January, are utilized in this analysis to provide a required value of the hydrogen/oxygen ratio.

[15] The ion distribution retrieved using the above mentioned customized method (Appendices A and B) from NUADU data integrated over 30 min from 2330 UT on 21 January is compared with a distribution derived from contemporaneous HENA data using the well-established, inversion method of *DeMajistre et al.* [2004] [see also *Vallat et al.*, 2004]. The retrieved ion distributions are in addition compared with in situ ion measurements made by the Hot Ion Analyzer (HIA) aboard the Double Star spacecraft TC-1 [*Reme et al.*, 2005] from 1600 UT to 0900 UT, 21–22 January. This instrument measured particles between 5 eV/q and 32 keV/q with high time resolution but without mass discrimination. In section 4.3, correspondences and differences between the NUADU, HENA, and HIA data are discussed.

[16] An account of modeling the various current systems that contribute to the *Dst* index is provided in section 5.1. This methodology is applied in section 5.2 to determine the nature of the contributions made by external sources during the geomagnetic storm of 21–22 January 2005, and the

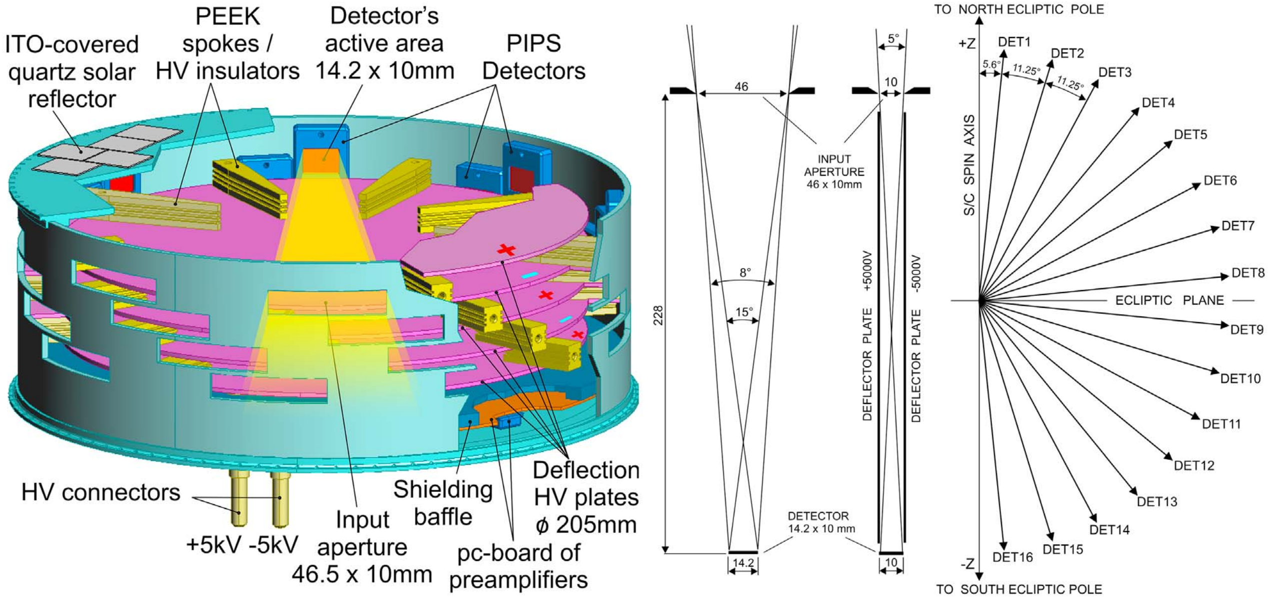

Figure 3. (left) Virtual model of the NUADU sensor head showing several of the apertures of sixteen Passivated Implanted Planar Silicon (PIPS) detectors which are mounted at four different heights. Each aperture is 228 mm away from its corresponding sensor. (ITO stands for Indium Tin Oxide; PEEK is an acronym for polyether ether chloride as well as a corresponding commercial brandname from the Victrex Company). (right) FOV definition of a single detector and the pointing directions of all 16 detectors which each have equal fields of view [11.5° × 2.5° (fwhm)] regularly distributed over an 180° angle in the elevation plane. The spin of the spacecraft allows the azimuthal plane to be divided into 128 equal sectors through counting pulses provided by the onboard Spin Segment Clock. The full 4π solid angle is, thereby, divided into $16 \times 128 = 2048$ pixels. For further details see the text.

results obtained are also discussed. In section 5.3 a model of the changing magnetic field is compared with the ENA measurements and correspondences between this model and the observations considered. Finally, section 6 contains a summary of the conclusions reached.

2. ENA Production and Detection

2.1. ENA Production

[17] Energetic neutral atoms (ENAs) are produced in the Earth's magnetosphere through charge exchange between singly charged magnetospheric ions and atoms of the exosphere. Only a few electron volts of energy are lost during a typical, resonant, charge exchange and, in consequence, an ENA formed in this way effectively retains the energy and momentum it had at the moment of the neutralization of its antecedent ion. Hydrogen and oxygen ENAs which comprise the dominant local products of H^+ and O^+ charge exchange encounters span the energy range between a few eV and several hundred keV. Neutral atoms propagate with typical velocities of several thousand km/s and, being effectively unimpeded by local gravitational fields, they follow straight-line trajectories emanating from their sites of creation. By integrating such emissions along lines of sight that link the locations of ENA production to the viewing point of an ENA detector aboard a spacecraft, it is possible to form an image of the ENA emitting populations. The ENA flux measured in each pixel of an image is the line of sight integral (along the line of sight direction of the pixel) of the unidirectional ion fluxes, multiplied by the local density of the neutral exospheric gas and by the charge exchange cross section between the two species. The extraction of quantitative information from such images concerning their parent ion distributions requires image inversion (section 4). Analysis of a sequence of such images can yield information concerning ongoing dynamic changes in the ion population concerned.

2.2. NUADU Instrument on TC-2

[18] The NeUtral Atom Detector Unit (NUADU) on the Double Star–Polar spacecraft (TC-2) has the capability to detect energetic neutral atoms (ENAs) in the approximate energy range 30–200 keV. TC-2 was injected into an orbit with perigee altitude 558 km; apogee altitude 38362 km; inclination to the Earth's equator 89.88°; orbital period 11.5 h and spin period 4.1 s on 25 July 2004.

[19] NUADU was designed to remotely sense 4π distributions of energetic neutral atoms through employing 16 detectors and exploiting spacecraft spin. Figure 3 (left) shows a virtual model of the NUADU Sensor Head. Several of the sensors (Passivated Implanted Planar Silicon detectors/PIPS), which were individually mounted over four different heights, are illustrated in this representation. In the foreground, certain of the entrance apertures, each of which was located 228 mm away from its corresponding sensor, can also be seen. These apertures were covered by a fine shielding mesh (not illustrated) which was maintained at a voltage of –20 V. An electrostatic, high-voltage (±5 kV) deflection sys-

Table 1. Energy Channels of NUADU

Energy Channel	H (keV)	O (keV)	ΔE_H (keV)	ΔE_O (keV)	$\Delta E_H/E_H$ (%)	$\Delta E_O/E_O$ (%)
E1: TH1–TH2	~45–50[a]	–138[a]	30		86	
E2: TH2–TH3	50–81	138–185	31	47	47	29
E3: TH3–TH4	81–158	185–300	77	115	64	31

[a] TH1 is adjustable by telecommand.

tem was installed inside the Sensor Head to sweep away charged particles with energies <300 keV from the detectors.

[20] Each detector had a thickness of 300 μm, and all were operated at full depletion. A metalization layer (150 nm of Al) was deposited on each detector to render it impervious to both visible light and UV radiation. Each had a rectangular active area of 14.2 × 10 mm and they featured equal fields of view (11.5° × 2.5° fwhm), regularly distributed over an 180° angle in the elevation plane. The geometric factor was 0.0125 cm^2 sr per 11.5° × 2.5° pixel and the total geometric factor was 0.20 cm^2 sr. Figure 3 (right) illustrates the field of view (FOV) of a single detector and the pointing directions of all 16 detectors.

[21] The spacecraft spin (4 s) allowed the azimuthal plane to be divided into 128 equal sectors through counting pulses provided by the spacecraft Spin Segment Clock interface. The full 4π angle was divided, accordingly, into 16 × 128 = 2048 pixels and, at the 4 s spacecraft spin period, the integration time of each pixel was 31.25 ms. NUADU had the capability to provide a full 4π image on the completion of each spacecraft spin in synchronization with the Sun Reference Pulse provided by the spacecraft. It was possible to integrate (N) spins onboard over a range N = 1–32. Further integration of the images can be performed on the ground to improve the count statistics.

[22] The NUADU Sensor Head was calibrated using neutral atom beams generated at different energies within a 30 m diameter ring accelerator. The objective of the procedure was to decide, on the basis of the responses of the detectors, on appropriate threshold values for the four discriminators that determined the energy channels of NUADU. It was found from plots showing how the voltage pulse amplitudes were related to particle energy that if E is in keV and V is in volts, then for H,

$$V = (0.00496682 \times E_H) - 0.156747, \quad (1)$$

and for O,

$$V = (0.00330185 \times E_0) - 0.364899. \quad (2)$$

[23] Setting of the discriminator thresholds on the basis of the calibration measurements involved taking into account a number of factors including providing overlapping as far as was feasible with the energy channels of IMAGE with a view to performing future complementary observations.

[24] Table 1 presents the energy bands and discriminator thresholds selected for NUADU. Of these, the setting of Threshold 1 could be varied on orbit by telecommand to allow it to be set above the prevailing noise level. The background experienced during commissioning required the setting of this threshold at 45 keV. More detailed accounts of NUADU are contained in the work of *McKenna-Lawlor et al.* [2004, 2005a].

2.3. HENA Instrument on IMAGE

[25] The IMAGE spacecraft was launched into an elliptical polar orbit on 25 March 2000 with apogee altitude 45,922 km and perigee altitude 1000 km. Apogee was initially at 40° north latitude. The apogee of IMAGE precessed during its first year in orbit from latitude 40° to 90°. Thereafter, through continuing to precess, it repeatedly returned to, and passed through, the initial location of its apogee. The spacecraft completed an orbit every 14.2 h.

[26] The High-Energy Neutral Atom (HENA) instrument aboard the IMAGE spacecraft was designed to determine the velocity, trajectory, energy and mass of ENAs in the 10–200 keV energy range and, from these data, images of ENA source regions in the inner magnetosphere can be constructed. Inside the sensor head alternately charged deflection plates were mounted in a fan configuration in front of the entrance aperture. The velocity of an incoming ENA could be determined by measuring its time of flight (TOF) from the entrance slit either to the back foil and 2-D imaging microchannel plate (MCP) detector or to a solid state detector (SSD). When an incoming ENA passed through the entrance foil it produced secondary electrons which were accelerated and steered to the front imaging MCP. This provided the start signal for TOF analysis while also registering the position at which that ENA had penetrated the entrance slit. Thereafter, the ENA continued through the sensor to the backplane where it impacted either the foil in front of the 2-D imaging MCP or the SSD. In the former case, secondary electrons ejected from the back foil triggered a stop pulse in the 2-D imaging MCP while also registering the position of the incident ENA. If the particle struck instead a pixel of the SSD, secondary electrons ejected by this impact were steered to the "coincidence" MCP which provided the TOF stop signal while the position of impact was registered by the SSD itself. The geometric factor was ~1.6 cm^2 sr and the efficiency was ~0.2 for H and 0.9 for O.

[27] The start and stop pulses provided the time of flight of the ENA while the position measurements revealed its trajectory and path length within the sensor, thereby allowing the velocity of the particle concerned to be calculated. When an ENA impacted the SSD it generated a current pulse. The amplitude of this pulse (pulse height) was directly proportional to the amount of energy that the ENA deposited in the SSD. Particle velocity could be determined from TOF data. Once the energy and velocity of an ENA is determined, its mass can be calculated. The determination of mass from the velocity and SSD energy measurements constituted the primary technique employed in analyzing

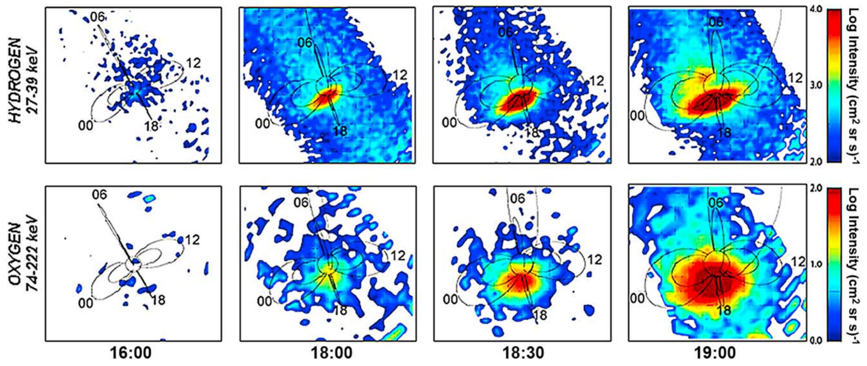

Figure 4. Images of the ring current event of 21 January 2005 recorded in ENAs between 1600 and 1900 UT by the HENA instrument aboard IMAGE, when the spacecraft was traversing the Southern Hemisphere: (top) hydrogen 27–39 keV and (bottom) oxygen 74–222 keV. The observations ended when IMAGE entered the radiation belts at 1920 UT. Both the hydrogen and oxygen images indicate that a strong substorm injection began between 1600 and 1800 UT. For details of the format employed, see the text.

HENA data to determine ENA composition. A second technique used the pulse height of the MCP signal to distinguish between O and H, the two most common neutral atoms present in the magnetosphere. The instrument rejected energetic ions ≤500 keV/charge, thereby allowing ENA images to be obtained in the presence of ambient energetic ions. Each measured ENA was added to an accumulating ENA image according to its species, velocity and trajectory. A map of the sky was maintained in memory and each particle was binned into the image pixel of that map according to the time of its detection (with millisecond resolution). High-velocity images were binned at 3° resolution and lower velocity images at 6° resolution (over sampling). The instrument was designed to return images of the HENA emitting regions of the inner magnetosphere with 2 min time resolution at an angular resolution of 8° for particles above ~50 keV/nucleon. Further details are contained in the work of *Mitchell et al.* [2000]. It is noted for comparison that the energy channels of IMAGE/HENA included the following: E3: 27–39 keV, E4: 39–50 keV, E5: 50–60 keV, E6: 60–81 keV, E7: 81–119 keV, E8: 119–198 keV and E9: >198 keV.

3. ENA Observations and Contemporary Geomagnetic Variations

3.1. Observations of the Ring Current (21–22 January 2005)

[28] NUADU/TC-2 and HENA/IMAGE were at orbital locations (Figure 2) that allowed each instrument to image the ring current from different vantage points during the main phase of the geomagnetic storm on 21–22 January 2005. TC-2 was inside the radiation belts when a CME related shock wave produced a large pressure pulse at the magnetopause at ~1712 UT on 21 January (section 1.2) and, in consequence, NUADU was not in operation at that time. IMAGE was, however, situated outside the radiation belts, and Figure 4 presents two sequences of measurements obtained by HENA between 1600 UT and 1900 UT. These data comprise hydrogen images (energy range 27–39 keV; Figure 4, top) and oxygen images (energy range 74–222 keV; Figure 4, bottom) individually recorded at 1600 UT, 1800 UT, 1830 UT, and 1900 UT. The plots are displayed in an equidistant, azimuthal projection which presents close to what a human eye would see. During these observations IMAGE was in the Southern Hemisphere and viewed toward the Northern Hemisphere. When the spacecraft entered the radiation belts at 1920 UT the microchannel plate (MCP) bias automatically switched off and observations ceased. It is noted that the broad bands of emission seen to extend diagonally across the hydrogen images in Figure 4 indicate the ambient presence of high-intensity, charged particles (due to the close proximity of the spacecraft to the radiation belts during the taking of these measurements). IMAGE emerged from the radiation belts at 2300 UT on 21 January, and HENA then recorded ring current data (Figure 5) until ~0130 UT on 22 January. TC-2 exited the radiation belts at 2330 UT on 21 January and NUADU, thereafter, secured images of the ring current up until 0219 UT on 22 January. The next time that TC-2 emerged from the radiation belts, at 1030 UT on 22 January, no significant ENA signal was present in the ring current region.

[29] During low perigee passes of TC-2 when the spacecraft had an altitude <5 R_E, grid system discontinuities within NUADU gave rise to spurious maxima in the data. In the case of observations made from ~0130 UT, on 22 January, not only was this effect present but it was exacerbated by the then orientation of the spacecraft toward the Sun, such that low-altitude ring current emissions which, primarily, were recorded by Detector 16 were mixed with the Sun Pulse signal. Thus, the observations made from 0130 UT were not reliable and are not presented here, although it was possible to discern that ring current activity was still in progress up to 0219 UT. Figures 6a–6c present NUADU data integrated over three 30 min intervals) between 2330 UT on 21 January and 0130 UT on 22 January in energy channel 2 (which measures 50–81 keV hydrogen atoms and 138–185 keV oxygen atoms, without mass discrimination). The elevation scale is indicated by closed, dashed, white rings, and the azimuth scale is indicated by labeled, dashed lines. The color scale indicates the logarithm of particle counts. Solid white curves represent constant

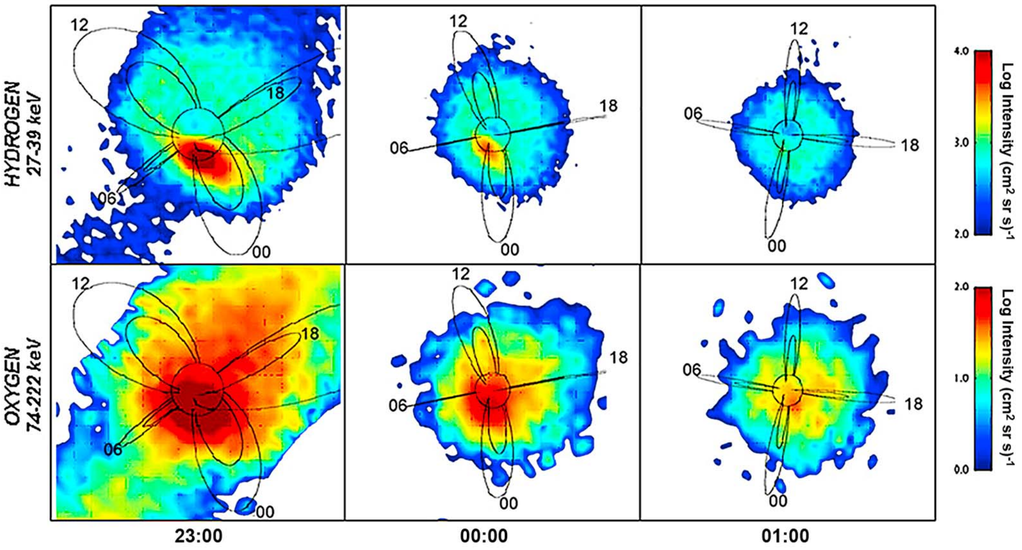

Figure 5. Images of the ring current recorded in ENAs by the HENA instrument aboard IMAGE in hydrogen and oxygen between 2300 UT on 21 January and 0100 UT on 22 January 2005, when the spacecraft was traversing the Southern Hemisphere: (top) hydrogen 27–39 keV and (bottom) oxygen 74–222 keV. For details of the format employed, see the text.

L values (L = 4, 8). Four local times are shown in red. The position of the spacecraft during the measurements is indicated at the bottom of the plot in units of R_E and in GSM coordinates. The ENA count maximum on the nightside was distributed in a narrow region with a rather sharp boundary close to the profile of the Earth, which is represented by a solid white ring. The bright region is interpreted to be due to ENA emissions from the magnetic L shells external to L = 4.

[30] At 1600 UT on 21 January, approximately 1 h before the arrival of the pressure pulse, the HENA images displayed a "quiet ring" in hydrogen and oxygen (Figure 4). At 1800 UT when the next images were available, the records show that ring current activity had already commenced in hydrogen. The available sequence of observations indicates that the ring current region experienced a relatively large injection of both H$^+$ and O$^+$ at <1830 UT. Injection and energization continued up until at least 1920 UT when IMAGE entered the radiation belts and temporarily ceased to make observations.

[31] The presence of a strong positive increase in *AE* (Figure 1, first panel) with maximum at ~1800 UT indicates that dipolarization occurred in the magnetotail. Further, measurements made aboard GEOTAIL (which was located in the magnetosheath) showed that during the interval 1851–2010 UT the magnetic tilt angle rotated twice between ~ − 45° and +45° owing to local variations in Bz [*Du et al.*, 2008], and this also suggests that the magnetic field in the plasma sheet changed from a tail like to a dipolar configuration. The ambient proton fluxes increased within the same period by a factor of 2. ENA data (Figure 4) show that the ring current images from 1800 to 1920 UT were asymmetric and that they displayed no visible symmetric part.

[32] An ENA record obtained at 2300 UT on 21 January by HENA/IMAGE when the spacecraft exited the radiation belts (Figure 5) shows that the oxygen component was especially strong at that time. These emissions, which are interpreted to be produced when O$^+$ ions mirror/precipitate at low altitudes [*Mitchell et al.*, 2003], provide evidence that oxygen played a role during this part of the event in contributing to magnetospheric filling. Oxygen emissions waned thereafter (most likely due to charge-exchange losses) and had virtually disappeared by ~0100 UT on 22 January.

[33] Three NUADU images (Figures 6a–6c) recorded from 2330 UT on 21 January employing 30 min integration times show that the ring current remained substantially disturbed up until at least 0130 UT on 22 January. Light contaminated records (not presented) obtained up to 0219UT indicate that disturbances within the ring current were still ongoing up to at least the latter time. Meanwhile substorm activity did not subside except during a rather short time interval (2330–0110 UT on 21–22 January and at around 0200 UT on 22 January.

3.2. Geomagnetic Data (21–22 January 2005)

[34] Two processes are generally suggested to explain ring current disturbances: namely, (1) substorm particle injections and (2) transport and energization of plasma sheet particles by the enhanced convection electric field. As pointed out by *Lyons and Schulz* [1989], the latter process is in particular capable of energizing ring particles located at L < 4, especially if the electric field fluctuates.

[35] *Du et al.* [2008] employed the integrated interplanetary electric field (ΣEy) to represent the input of energy to the magnetosphere from the solar wind (with speed V) such that

$$Ey = -V \times Bs, \tag{3}$$

where Bs = -Bz if IMF Bz < 0 and Bs = 0 if IMF Bz = 0.

[36] These authors considered that integrated SYM-H (ΣSYM-H) represents the accumulation of energy in the ring current. For convenience, a plot by *Du et al.* [2008]

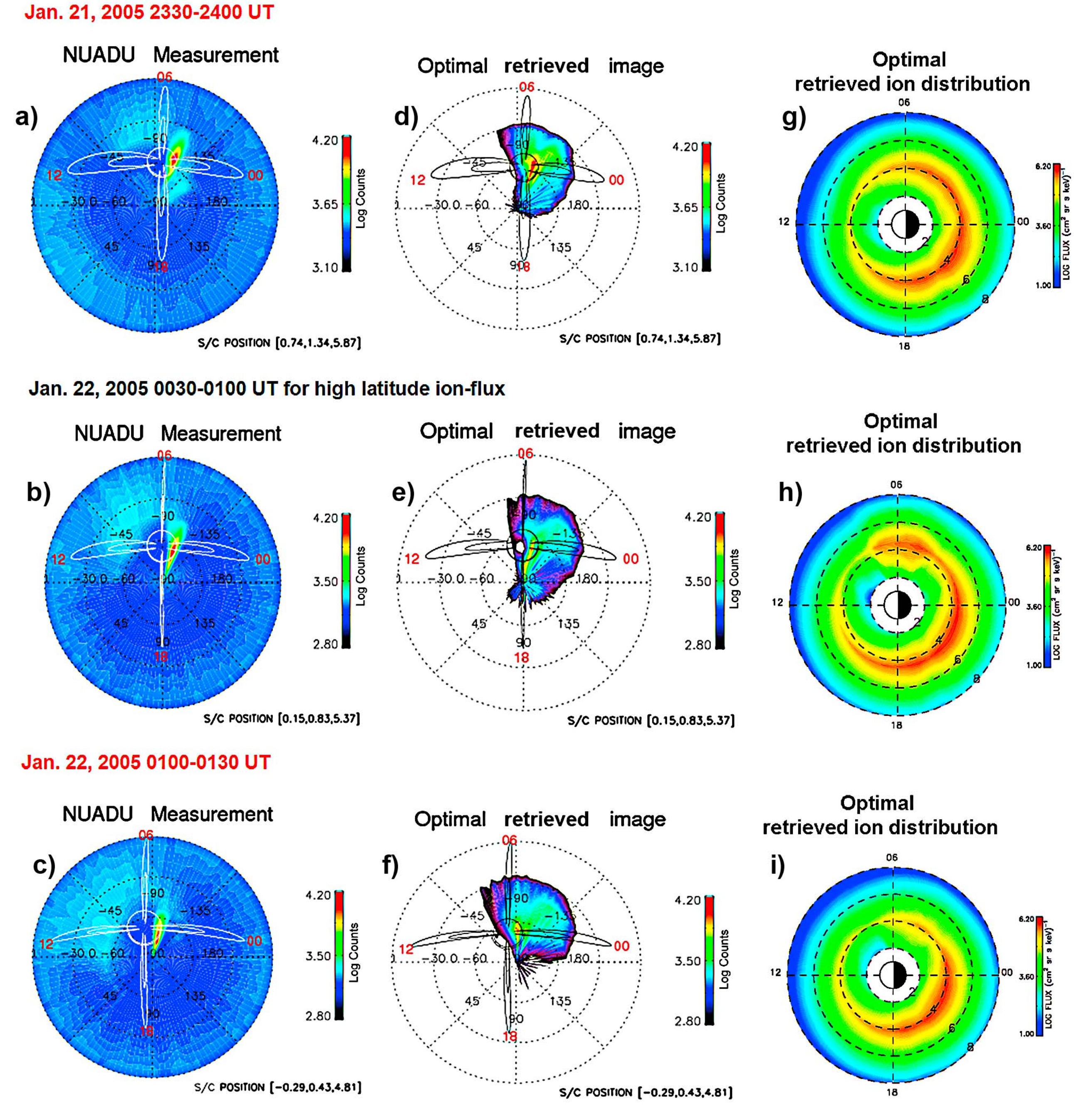

Figure 6. (a–c) Three ENA images recorded in energy channel 2 (50–81 keV) by the NUADU instrument integrated between 2330–2400 UT, 0030–0100 UT, and 0100–0130 UT, 21–22 January 2005. The elevation scale is indicated by closed dashed white rings, and the azimuth scale is indicated by (labeled) dashed lines. Two sets of geomagnetic dipole field lines (solid white curves) are plotted at noon (1200 LT), dusk (1800 LT), midnight (0000 LT), and dawn (0600 LT). Local times are shown in red. The altitudes of the field lines at the equator are 4 R_E and 8 R_E. The color scale indicates the logarithm of integral energy particle counts. In each case, the position of TC-2 is indicated (bottom right) in R_E/GSM coordinates. (d–f) Corresponding optimum recovered images obtained using constrained linear inversion by iteration (Appendix B). (g–i) Corresponding optimum ion distributions retrieved from the observations.

showing the temporal variations of ΣEy and ΣSYM-H during the January 21–22 activity is reproduced (with minor modifications) in Figure 7. This latter figure shows that, in the period spanning the arrival at the magnetopause of a shock at 1712 UT (vertical line Sh) and the later arrival of a discontinuity at ~1843 UT (vertical line D) ΣEy increased whereas ΣSYM-H remained at a low value until ~1946 UT. At this juncture when Bz turned northward (vertical line

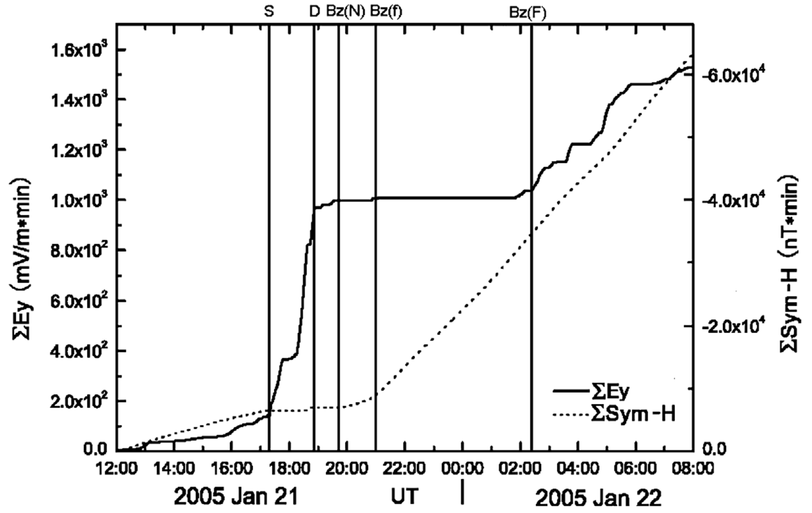

Figure 7. Variations in ΣEy and ΣSYM-H in the interval 1200 UT, 21 January, to 0800 UT, 22 January. For details, see the text. Figure 7 is based on the work of *Du et al.* [2008].

BzN), ΣEy became horizontal while ΣSYM-H showed a well-defined rise. From 2101 UT on 21 January until 0224 UT on 22 January Bz was small, positive and displayed minor fluctuations. From 0224 to 0612 UT Bz showed fluctuations (±10 nT) that extended southward. These were accompanied (Figure 7) by fluctuating increases in ΣEy while also ΣEy and ΣSYM-H increased in tandem. Although *Dst* which was, meanwhile, in course of development continued to decrease for more than 11 h after Bz turned northward at 1946 UT on 21 January, this was not a monotonous descent but, rather, followed the changing patterns of Bz until this component effectively settled close to zero between ~0600 and 0700 UT (Bz varied only very slightly thereafter).

3.3. Discussion of Contemporary ENA and Geomagnetic Data

[37] It was conjectured by *Du et al.* [2008] that a possible (although not the only conceivable) scenario to explain the data in Figure 7 is that the interval spanning shock arrival (Sh) at 1712 UT up to the strong northward turning of Bz at 1946 UT (Bz (N)) was a period when a large amount of solar wind energy entered the magnetosphere at times when Bz was southward directed (note that for a considerable interval around 1800 UT Bz was positive). The period 1850–1946 UT that *Du et al.* [2008] pointed out was characterized by a tilt angle near to zero was interpreted by these authors to constitute an energy-storing phase. In addition, the interval ~1850–0140 UT (21–22 January) was deemed to constitute an energy-releasing phase (comprising a slow unloading process) in the course of which energy stored in the magnetosphere was converted to the kinetic energy of particles in the ring current.

[38] It is well known through many studies [e.g., *Thomsen et al.*, 1998] that next in importance to the influence of Bz, plasma sheet density constitutes a crucial preconditioning parameter with regard to regulating the eventual intensity of storm-time ring current. In the present case the very high speed, ambient, solar wind (Figure 1, second panel) and high dynamic pressure (Figure 1, fourth panel) that pertained up until the early hours of 22 January, would have stimulated enhanced local convection so that, in consequence, a substantial quantity of (mostly ionospheric) plasma sheet material was available for the ring current. The ongoing fluctuations recorded in Bz up until ~0600 UT on 22 January would then have acted to support trapping and energization of this plasma sheet material leading gradually to a symmetric, long-lived, storm time ring current.

4. Ion Distribution Retrieval Methods

4.1. Classical Ion Distribution Retrieval Methods

[39] ENA data can be analyzed in several ways to reconstruct the ion distributions present in the inner magnetosphere around the magnetic equator plane. One, described by *Roelof* [1987] and by *Roelof and Skinner* [2000], involves forward modeling of the concerned plasma volume. According to this technique, the parameterized ion flux is combined with a geocoronal hydrogen model and line integrated to derive the ENA image intensities at the location of the measurement. The modeled ENA flux is then passed through the telescope function of the recording instrument so that a direct pixel by pixel comparison can be made between the predicted and measured values. This process is continued iteratively by varying the parameters defining ion fluxes until a "best match" is achieved between the predicted and measured values. Experience shows that there is generally a rapid convergence between the predicted and the measured ENA fluxes. Another way to retrieve the ion distributions described by *Perez et al.* [2000, 2001] uses cubic B-splines as local functions describing ion distributions in a constrained, linear retrieval procedure. At the present time, a systematic analysis of the accuracy of the latter method has not yet been developed.

[40] Yet another means of retrieving the parent ion distribution in the equatorial plane is a constrained linear inversion method which involves the utilization of global functions to represent the shape of the ion distribution in the magnetosphere. The parameters adopted in these functions are incorporated in a nonlinear, least squares fitting algo-

rithm to provide an optimum fit to the measured data. A problem with this method is that, because of the limited number of free parameters available, the model is unable to reproduce all the shapes that the ion distributions can potentially assume. However, a judiciously selected linear set of functions can accommodate a reasonably wide range of spatial structures while maintaining simple methodology [*Twomey*, 1977; *Brandt et al.*, 2002; *DeMajistre et al.*, 2004]. Measured ENA count rates (j_{ENA}) (expressed in units of the number of ENAs per unit area, per solid angle, per unit time, per unit energy) are represented in this method by a line of sight integral over the ion flux (j_{ION}) and the number density (n) of the cold neutral gas in which the plasma is submerged, multiplied by the relevant charge exchange cross section (σ_{10}):

$$j_{ENA}(E) = \int_0^\infty j_{ION}(E,l) n_l \sigma_{10}(E) dl. \tag{4}$$

[41] To obtain the underlying ion distribution, the ENA count rates are expressed as linear sums of the ion fluxes present in the equatorial plane (i.e., the ion flux is expanded into a summation over those ion fluxes contained in spatial bins within the equatorial plane). The inversion algorithm employed incorporates a magnetic field and an exospheric model and a constrained inversion technique is applied. Validation of this method is achieved through comparing ion fluxes retrieved by inverting HENA/IMAGE data with contemporaneous in situ ion measurements made in the magnetosphere [*Vallat et al.*, 2004].

4.2. Method of Ion Distribution Retrieval Customized for NUADU Data

[42] More recently, a method customized for NUADU data, which during ring current disturbances feature spatially sharply peaked bright emissions, was developed to retrieve the parent ion distributions [*Lu et al.*, 2008]. The ENA images utilized in this procedure are first cleaned to (1) remove effects due to solar photons, (2) balance statistically noise responses between different detectors, and (3) correct polar overlaps in the fields of view of certain detectors. It is noted that, when the responses of individual sensors were investigated during prelaunch calibrations they were found to be closely similar (such variations as were present merely reflected slight differences in the thicknesses of the applied metallization and dead layers [*McKenna-Lawlor et al.*, 2004]). Post launch, changes in the noise levels in certain of the detectors were noted and it is presently required to balance these changes statistically. Appendix A contains an account of the steps used to clean NUADU data.

[43] NUADU images cover a 4π solid angle and only less than half of the pixels are related to ENA emissions from Earth. Thus, ENA counts below the average mainly represent noise fluctuations while pixels featuring above average counts indicate the presence of intense ENA emissions. In the records considered below, the mean noise background (azimuth region 60°–140° and elevation region 0°–100°) was 110 counts and the average count for all pixels over 4π was 240. On implementing the procedure described in Appendix A with respect to cleaning selected NUADU records, the noise background was reduced to less than 1% of the ENA maximum (which is an acceptable value for successful ion flux inversion).

[44] The method of ion distribution retrieval developed for the NUADU data set is described in Appendix B. In brief, the basic equations used incorporate: the NUADU response function, an empirical ion flux model and an exospheric neutral distribution. A classical method of constrained linear inversion developed by *DeMajistre et al.* [2004] was at first utilized in which the data inversions obtained at different constraint strengths were iteratively compared with the corresponding measurement covariance until a minimum value was found (indicating that an optimum value of the relative error had been obtained). However, it was found that, when this methodology was applied to NUADU data (which typically feature a spatially sharply peaked intensity distribution) the solution obtained tended to oscillate and even present negative values. Also, the strong coefficient of constraint associatively employed smoothed the inversion result too much relative to the measurements.

[45] To overcome these problems an iterative technique, also based on constrained linear inversion but in which the inversion results were compared directly with the measurements rather than with the measurement covariance, was implemented. These comparisons were made pixel by pixel, using only counts above the noise level at constant constraint strength. While the minimum relative error achieved in this way depends on the number of pixels taken into account in the statistics, for NUADU data this value was found to be consistently lower than that obtained using the classical method of *DeMajistre et al.* [2004].

4.3. Comparison of Ion Distributions Obtained From NUADU, HENA, and HIA Data

[46] Figures 6a–6c show three integrated (30 min) measurements obtained by NUADU between 2330–2400 UT; 0030–0100 UT and 0100–0130 UT, on 21–22 January, 2005. In the absence of mass differentiation [*McKenna-Lawlor*, 2005b], it is necessary in the deconvolution procedure to assume, or have available, a value for the flux ratio that pertained between hydrogen and oxygen ions during each event analyzed. In the case of the data recorded on 21–22 January 2005, a value for this ratio is available from in situ magnetospheric measurements made by the RAPID instrument [*Wilken et al.*, 1997] aboard the Cluster spacecraft on 22 January (between ~2000 and 2300 UT at E > 27 keV and E > 90 keV, section B6]. The mean measured integral heavy ion flux (mostly oxygen ions) averaged over 4π (E > 90 keV was about 5.7×10^4 $s^{-1}sr^{-1}cm^{-2}$ while the mean measured integral proton flux averaged over 4π (E > 27 keV) was 4×10^5 $s^{-1}sr^{-1}cm^{-2}$. This ratio of ~7 was maintained during an evolution in the overall ion composition that was monitored by RAPID during the remainder of the day. The utilization in the present analysis of an ion ratio from in situ measurements made on the same day but at a later time than the ENA measurements should be related to the observation that, although maximum oxygen emissions were detected by HENA at 2300 UT on 21 January, by 0100 UT on 22 January the intensity of oxygen emissions had substantially subsided (Figure 5). Since the H^+/O^+ ratio is known to be highly variable during the first phases of a storm [*Daglis et al.*, 1999], it is noted that our adoption here

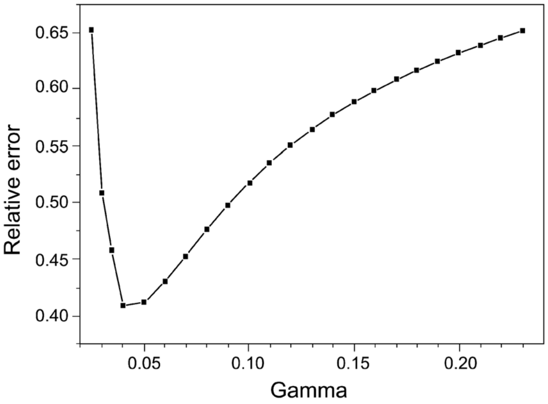

Figure 8. Relative error variance at $\gamma = 0.04$ monitored during the analysis of NUADU data recorded over a 30 min integration period from 2330 UT on 21 January 2005.

of a constant ratio based on the uniquely available Cluster data is only appropriate for a first-order analysis of a moderate storm and hence this is not an ideal (or standard) procedure.

[47] Figures 6g–6i show the optimum equatorial ion distributions with pitch angle 90° retrieved from each of the three integrated NUADU measurements (Figures 6a–6c) using the method outlined in section 4.2 and described in detail in Appendix B. In the representative case of the distribution retrieved from data recorded in the interval 2330–2400 UT, 21 January, on comparing the inversion results directly with the measurements while employing a value of the constraint strength $\gamma = 0.04$, a minimum relative error of 0.41 was obtained (Figure 8). The ENA image retrieved using the ion distribution of the linear inversion (Figure 6d) and the measured image (Figure 6a) match each other reasonably well with the most intense patch in the retrieved image located in the post dusk sector (L = 4) where, as in the measured data, it displays a sharp boundary. The maximum intensity of the optimal retrieved equatorial ion flux approached 1.2×10^6 s^{-1} sr^{-1} cm^{-2} keV^{-1}. The optimal ion distribution retrieved for the period 0030–0100 UT, 22 January (Figure 6h) was obtained at constraint strength $\gamma = 0.04$ with minimum relative error 0.44. The distribution at 0100–0130 UT, 22 January (Figure 6i) was obtained at constraint strength $\gamma = 0.04$ with minimum relative error 0.4.

[48] In Figure 9a, the optimum ion distribution retrieved from NUADU data recorded in Channel 2 (50–81 keV for H) between 2330 and 0100 UT, 21–22 January, is displayed beside an ion distribution retrieved from contemporaneous HENA data recorded in the energy range 60–119 keV (Figure 9b). The HENA ion distribution was retrieved using the method of *DeMajistre et al.* [2004]. Figure 9c presents the contemporaneous isotropic proton pressure (on a logarithmic scale) derived from HENA data. Figure 9d shows hydrogen energy densities recorded between 1600 UT, 21 January, and 0900 UT, 22 January, by the Hot Ion Analyzer

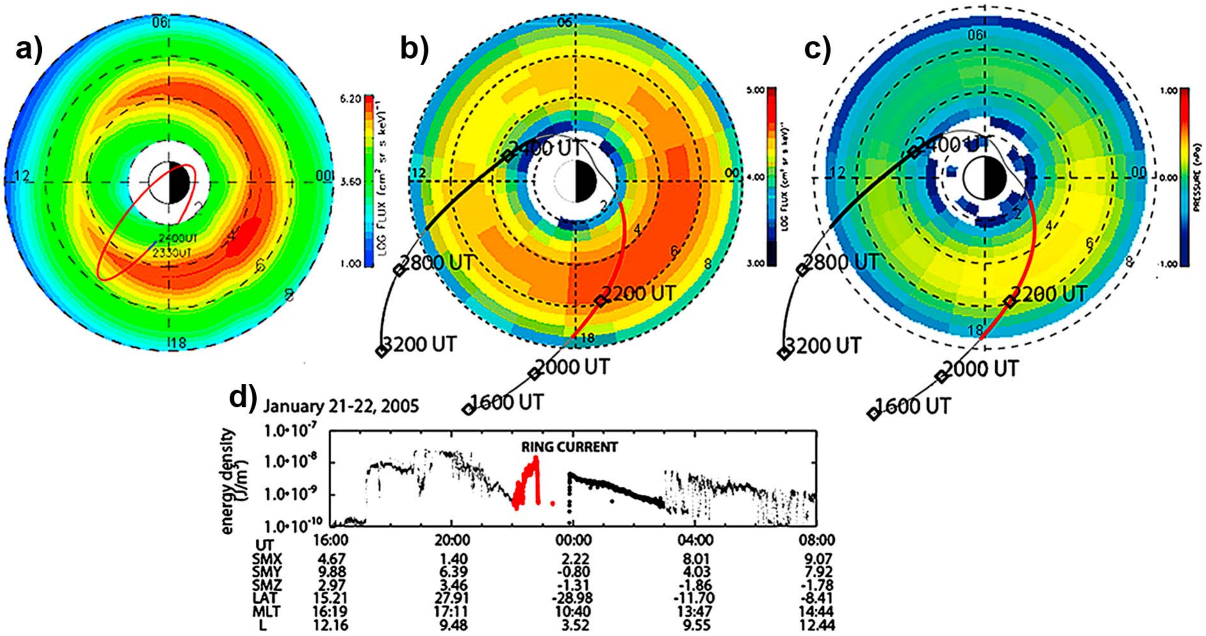

Figure 9. (a) Optimum hydrogen ion distribution retrieved from NUADU data (50–81 keV) integrated over 30 min from 2330 UT on 21 January 2005. (b) A contemporaneous hydrogen ion distribution retrieved from HENA data (60–119 keV). (c) Contemporaneous plot (on a logarithmic scale) of isotopic proton pressure obtained from HENA data. The Sun is on the left. (d) Energy densities < 32 keV/q measured by the Hot Ion Analyzer (HIA) instrument aboard the TC-1 spacecraft from 1600 UT, 21 January, to 0900 UT, 22 January. The red orbit track (L, Φ) of TC-1 superimposed on the HENA plots corresponds to the red data points in Figure 9d, where the maximum energy density was identified. It is noted that the orbit of TC-2 shown in MLT coordinates has a high L value when the spacecraft is near the cusp and a low L value near the equator.

(HIA) flown on the TC-1 spacecraft which recorded ions between 5 eV/q and 32 keV/q at high time resolution (4 s) but without mass discrimination [*Reme et al.*, 2005; *Dandouras et al.*, 2009]. The red orbit track (L, Φ) of TC-1 superimposed on the HENA plot corresponds to the red data points in plot (d), thereby highlighting the ring current crossing during maximum energy density.

[49] The NUADU and HENA ion distributions both feature less intense retrieved ion fluxes at dawn and this is attributed to ongoing losses through the magnetopause. The particle residence time in the magnetosphere can also contribute to particle loss in the dayside current sheet through charge exchange interactions (which are favored by a longer residence time). However, what the measured data show are not the ion gaps (also called "ion spectral gaps" or "stagnation dips") which usually appear in certain narrow energy bands around a "resonant" energy which is typically up to a few keV. An early study by *Buzulukova et al.* [2002] describes two types of such ion spectral gaps in the inner magnetosphere, and a more recent paper by *Vallat et al.* [2007] gives a detailed description of the observational characteristics and distribution of these features and presents a numerical modeling simulation study that reproduces their characteristics. The NUADU data were recorded at energies (E > 50 keV) well above the resonant energy between convection drift and gradient/curvature drift. Furthermore, Channel 2 of NUADU (50–81 keV) is much wider than any eventual resonant ion gap (whose effects would, consequently, be averaged out).

[50] It is pointed out that the retrieved ion distributions obtained from the two sets of ENA images using different methods show different flux values. Several factors are involved here. First, the images come from instruments (NUADU and HENA) which utilized energy channels with different thresholds. Charge-exchange cross sections (σ) are energy-dependent, and the energy thresholds concerned are in the steeply decreasing part of these curves. Thus, since J_{ENA} (E) is proportional to σ (E), even a moderate difference between energy thresholds can exert a strong influence on the measured ENA fluxes which were integrated over the energy ranges pertaining to the individual energy channels of each instrument. Under these circumstances the present study does not aim to produce cross-calibrated differential flux ranges (which would go beyond the characteristics of our instruments) but rather to deduce from the data the large scale topology of the ring current and its dynamic evolution. For this, integral ENA fluxes are appropriate and it is stressed that in the comparisons made between the data we only highlight shape agreement.

[51] Also it is noted that there are differences between the ways in which the two methods handle measured data. In the first instance the technique employed to retrieve ion distributions from NUADU measurements is based on a Kappa model whereas the DeMajistre method employs an exponent model. Second, the optimal result obtained in deriving the distribution presented in Figure 9a was obtained through comparing the inversion results directly with the measurements rather than with the measurement covariance (as is done in the case of the DeMajistre method). The former technique emphasizes the ENA maximum distribution and can result in obtaining higher values for the ion flux distribution than are obtained in Figure 9b, where the maximum ENA area is smoothed, thereby leading to an associated smoothing/lowering of the values derived. It is appropriate in view of these uncertainties regarding the "real" flux intensities to consider the values provided in Figure 9a to be in arbitrary units.

[52] Also, it should be emphasized that, although the ring current ion distribution extracted from NUADU/ENA data using the technique described in Appendix B shows gross features that correspond with the retrieval obtained from contemporaneous HENA data using the method of *DeMajistre et al.* [2004] with the ion differential flux decreasing at higher energies as expected, it is not anticipated that these distributions would be in full accord. In the first instance, as previously discussed by *McKenna-Lawlor et al.* [2005b], the look direction of an ENA imager aboard a particular spacecraft changes as that spacecraft follows its trajectory, thereby creating an illusion, due to the varying viewing geometry, that particular bright ENA emissions change their locations during the measurements. In the present instance this effect is compounded through comparing the observations of two spacecraft that followed different trajectories at different speeds over a 30 min period while viewing different hemispheres in slightly different energy regimes. Also, HENA provided separate images for hydrogen and oxygen, whereas NUADU, as mentioned earlier, does not support species separation.

5. Magnetic Field Modeling

5.1. Magnetospheric Magnetic Field Sources

[53] The *Dst* index for measuring magnetic storm intensity was originally thought to be well correlated with the inner ring current energy density [*Hamilton et al.*, 1988; *Greenspan and Hamilton*, 2000]. At the present time, however, it is recognized that *Dst* contains contributions from many sources [*Kalegaev et al.*, 2005, and references therein].

[54] N. A. Tsyganenko has over many years produced models [e.g., *Tsyganenko*, 2002a, 2002b] that provide a, semiempirical, best fit representation of the geomagnetic field based on a large number of satellite observations (e.g., IMP, HEOS, ISEE, POLAR, Geotail, etc). These models take into account the contributions from external magnetospheric sources (the ring current, magnetotail current system, magnetopause currents and the large-scale system of field-aligned currents). The latest versions of these models together with related software can be retrieved from http://modelweb.gsfc.nasa.gov/magnetos/data-based/modeling.html.

[55] Against this background, *Tsyganenko and Sitnov* [2005] developed a method (hereinafter TS04) to derive from contemporary magnetic field (IMF) and solar wind data the temporal variations of all the significant current systems that contribute to the geomagnetic field during major magnetic storms. The principal sources of the external magnetic field located in the magnetopause (cross tail current sheet, axisymmetric/partial ring currents and the Birkeland current systems) were each deemed to be driven by a separate variable W, defined as the time integral (from the beginning of the storm to the current moment) of the difference between the source and loss functions. In the

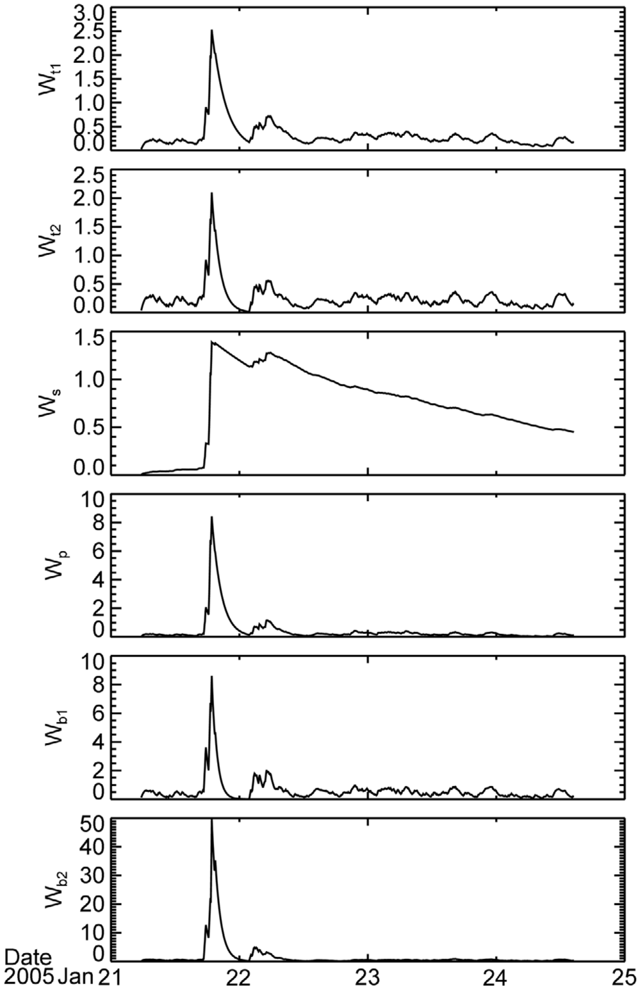

Figure 10. Six dynamical parameters (W_{t1}, W_{t2}, W_s, W_p, W_{b1}, and W_{b2}) modeled over the period 0540 UT, 21 January, to 1430 UT, 24 January 2005. For details, see the text.

TS04 model, the variables W, each for a particular current system, depend on the geoeffective parameters $N^{\lambda}V^{\beta}Bs^{\gamma}$, where N, V, and Bs denote the solar wind density, solar wind speed, and the magnitude of the southward component of the IMF, respectively. The power indices λ, β, and γ are unknown parameters of the driving function. Each source was assumed to have its own characteristic time scale and residual quiet time strength, and it was further considered that each partial contribution to the total field depended on the entire previous history of the external driving of the magnetosphere during a particular storm. All the parameters of the model free sources (i.e., their magnitudes, geometrical characteristics, solar wind/IMF driving functions, decay time scales and saturation thresholds) were treated as free variables, the values of which could be obtained from measured data. For more details, see Appendix C.

5.2. Modeling the Contributions of External Sources to the Storm of 21–22 January 2005

[56] The methodology of *Tsyganenko and Sitnov* [2005] was adopted in the present study to determine the contributions of significant, individual external sources during the magnetic storm of 21–22 January 2005.

[57] The measurements input to the model comprised IMF and Solar Wind (64 s averages) Level 2 data recorded simultaneously from 21 January 2005 aboard NASA's Advanced Composition Explorer (ACE). The ACE spacecraft orbits the L1 Lagrangian point (at ~0.01 AU Sunward of the Earth). Accounts of the ACE payload instruments and of the mission are contained in the work of *Stone et al.* [1998].

[58] The interval selected for analysis extended from 0540 UT on 21 January to 1430 UT on 24 January. This period, which covered all the important phases of the magnetic storm, had very few data gaps (maximum gap duration of 2 min). At other less important times very long data gaps pertained (up to 13 min). Data from the Magnetometer (Mag) and Solar Wind Electron, Proton and Alpha Monitor (SWEPAM) instruments flown aboard ACE (which are available at http://www.srl.caltech.edu) were combined and linearly interpolated in the analysis. Parameters extracted from this archive were: the proton density N (cm^{-3}); the alpha/proton ratio R; the proton speed V (kms^{-1}), the By and Bz components of the magnetic field in GSM coordinates (nT) and the X, Y, Z components of spacecraft position in GSE coordinates (km).

[59] The solar wind ram pressure P_d (nPa) input to TS04 was calculated using the expression

$$P_d = 1.67 \times 10^{-6} N V^2 (1 + 4R). \tag{5}$$

In cases where data concerning R were not available the expression

$$P_d = 2 \times 10^{-6} N V^2 \tag{6}$$

was substituted.

[60] The 64 s data were next shifted to the bow shock nose using a technique described in http://omniweb.gsfc.nasa.gov. In this regard, the associated time delay Δt (in seconds) was calculated using the following formula:

$$\Delta t = \frac{X}{V} \left\{ \frac{1 + Y\Gamma/X}{1 - Ve\Gamma/V} \right\}, \tag{7}$$

$$\Gamma = \tan(0.5 \arctan(V/428)), \tag{8}$$

where 428 (km/s) is the solar wind speed in the (-) GSE Y direction at Earth of an ideal IMF spiral line due to solar rotation and Ve is the speed of the Earth's orbital motion (30 km/s). Δt was added to the time at the position of ACE. From the data thus shifted 5 min averages were produced.

[61] The six dynamical parameters: W_{t1} (inner tail), W_{t2} (outer tail), W_s (symmetrical ring current), W_p (partial ring current), W_{b1} (Region 1 Birkeland current), and W_{b2} (Region 2 Birkeland current) in model TS04 were calculated using equation (C7). Figure 10 presents each of the six parameters modeled over the period 0540 UT, 21 January, to 1430 UT, 24 January. It is seen that all of them, with the exception of W_s (symmetrical ring current), were impulsive in nature and each displayed a slight enhancement on 22 January at ~2300 UT. W_{b2} (the Region 2 Birkeland current) was initially the dominant contributor.

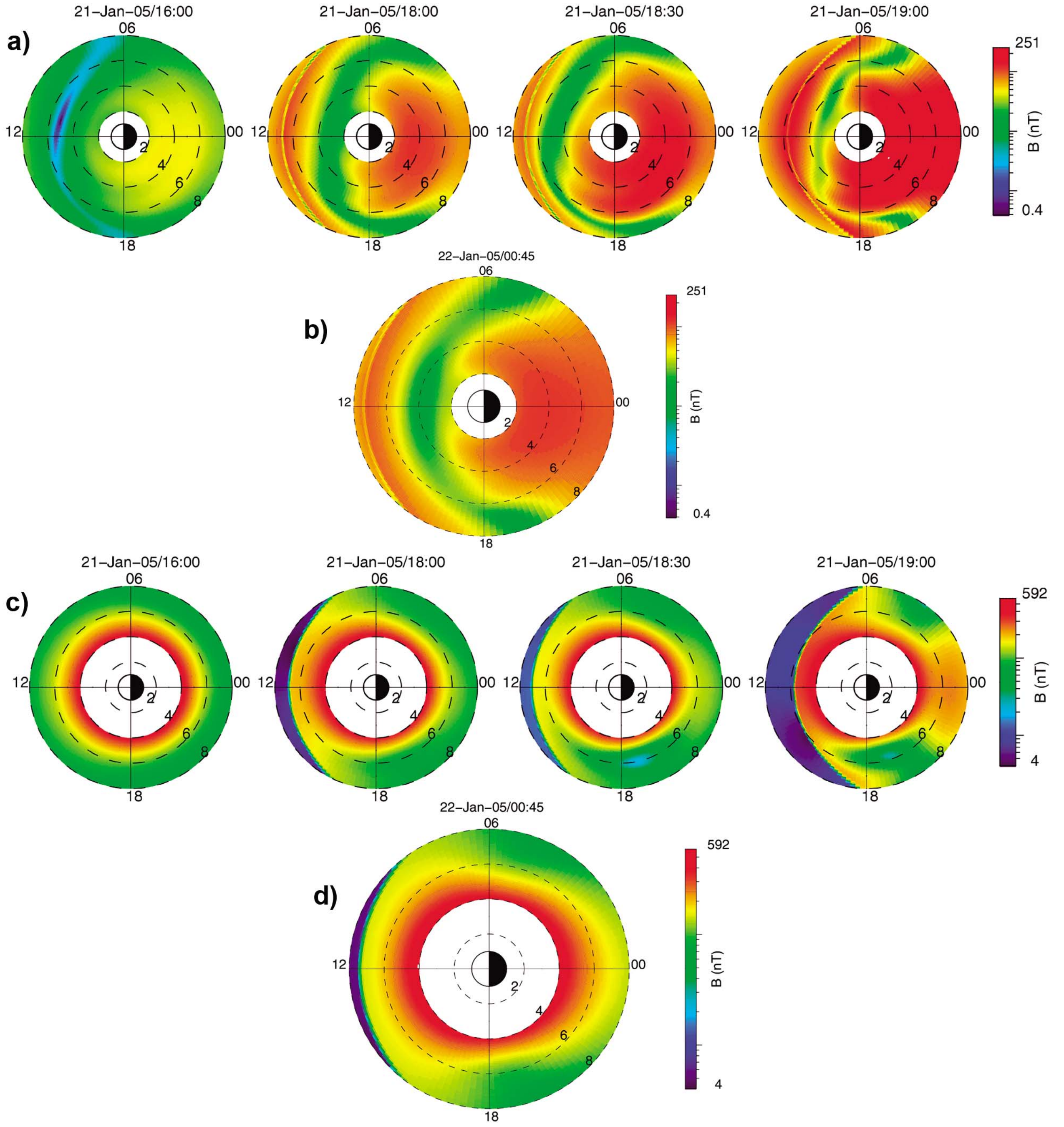

Figure 11. (a, b) The Tsyganenko (TS04) external magnetic field in the GSM equatorial plane plotted as a function of R and MLT (see the text) at various times during the development of the magnetic storm of 21–22 January 2005. (c, d) again the total (core plus external) magnetic field in the GSM equatorial plane is plotted as a function of R and MLT for the same times as before but only for values of R > 4 R_E.

W_s remained enhanced over several days. Also, Figure 10 demonstrates that at the beginning of the storm when the feeding rate of a current system overwhelms its losses, the variables W attained their highest values.

[62] *Dst* following the initial southward orientation of Bz at ~1712 UT on 21 January developed from 1946 UT under northward directed Bz, with minor positive fluctuations in Bz from ~2101–0224 UT, 21–22 January and variations that extended southward (in the overall range ±10 nT) from 0224 to 0612 UT on 22 January (section 3.2). Thus, although the magnetosphere was already disturbed at the commencement of the magnetic storm of 21–22 January owing to preceding solar activity (section 1.2) the magnitude of *Dst* was much less (minimum *Dst* = ~101 nT) than is typically the case in the aftermath of major solar activity such as that recorded on 20 January due to the predominantly northward orientation of Bz.

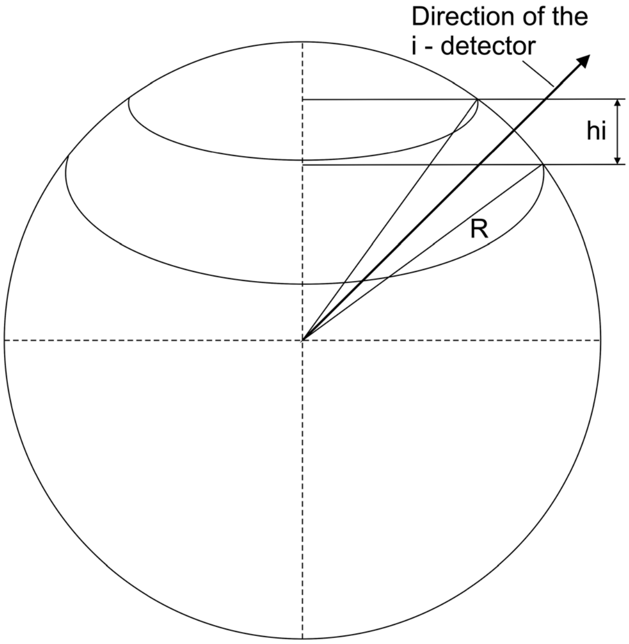

Figure 12. Plot showing how the scan area of each detector FOVi = $2\pi Rh_i$ depends on its distance from the spin axis. For details, see the text.

[63] The very slow decline in W_s (seen in Figure 10 to still be in progress on 24 January) may reflect the inferred availability (due to enhanced convection stimulated by the prevailing, high-speed, solar wind dynamic pressure) of substantial quantities of plasma sheet material in the ring current region which, through energization in the fluctuating field of Bz (up to ~0612 UT, 22 January) combined with transfer of energy from the magnetotail, is interpreted (section 3.3) to have sustained the disturbance over an extended time period.

[64] The value of W_{b2} computed for another storm on 6 April 2000 (minimum *Dst* = −288 nT), which also was characterized by a northward orientation of Bz, was very similar to that recorded during the storm of 21 January [*Kudela et al.*, 2008]. However, the peak values of all the other parameters were smaller during January 2005 by factors of 2–4 than those measured in April 2000. Also, the W values computed for the January event were lower than was the case during yet another comparable event on 20 November 2000.

[65] It is noted that the computed values of the parameters W are additionally of interest for checking the transmissivity of the magnetosphere with respect to low-energy cosmic rays during strong disturbances recorded by neutron monitors. Work in this regard is ongoing but preliminary studies [*Kudela et al.*, 2008] indicate that, at least for one geomagnetic storm, the parameters determined using TS04 give a more realistic estimate of cut-off rigidity changes than is provided by earlier magnetic models.

5.3. Comparisons Between Plots of the Modeled Magnetic Field and ENA Data

[66] Finally, comparisons between plots of the modeled magnetic field and ENA data recorded during the January 2005 event were carried out. To achieve this: the already calculated dynamical parameters W (which “remember” the prehistory of the magnetospheric configuration) and instantaneous values of: the *Dst* index (nT); the Geocentric Solar Magnetospheric Interplanetary Magnetic Field (GSM/IMF); the By and Bz components (nT) and the solar wind ram pressure P_d (nPa) were individually input to the TS04 model. The magnetic field vector in the GSM equatorial plane was then calculated using the spatial step 0.05 R_E (Earth radius) while also the GSM coordinates were transformed to the Solar Magnetic (SM) system, where 0° longitude corresponds to magnetic local time (MLT) noon [*Fränz and Harper*, 2002].

[67] The external magnetic field in GSM in the equatorial plane as a function of radial distance (R) and MLT (with $\Delta R = 0.1\ R_E$ and $\Delta MLT = 0.2$ h) was plotted at various times (Figure 11a, at 1600, 1800, 1830, and 1900 UT, 21 January, and Figure 11b, at 0045 UT, 22 January 2005). The 00, 06, 12, and 18 h of MLT are shown on each of these plots as well as the locations of radial distances 2, 4, 6, and 8 R_E. Also, the core magnetic field was computed for the same times using the IGRF-10 model (available at http://www.ngdc.noaa.gov/IAGA/vmod/igrf.html). This total (core plus external) magnetic field was plotted in the same format as that of plots a and b in plots c and d of Figure 11 where, since the total magnetic field did not change significantly below ~4 R_E, only the field at $R > 4\ R_E$ is displayed.

[68] Before the start of the magnetic storm a nearly symmetric model field distribution pertained with weak noon-midnight anisotropy above 5 R_E (Figure 11c). Temporal changes in the total magnetic field were due only to the time varying field of the external current systems whereas spatial variations resulted from the effect of the combined core and external fields.

[69] Figures 11a and 11c provide global views of magnetospheric conditions from 1 h before through the early development of the magnetic storm of 21–22 January 2005. Figures 11a and 11c are suitable for comparison with Figure 4, which shows sequences of ENA measurements obtained by HENA. Also, Figures 11b and 11d may be compared with the measurements made by HENA and NUADU displayed in Figures 5 and 6.

[70] Early enhancements in H and O were temporally associated with the intensification of external currents. The image recorded by HENA at 1830 UT shows that the ring current was strongly asymmetric when also (Figure 11) external current systems produced a strongly asymmetric magnetic field (with strong compression of the magnetosphere and dawn-dusk asymmetry at the beginning of the event).

[71] A progressive reduction in the asymmetry of the ring current was observed in HENA data (Figure 5) and by 0100 UT on 22 January only a slight asymmetry was still present. This observation is complementary to the still intensified but almost symmetrical, external modeled magnetic field of 0045 UT.

6. Conclusions

[72] A moderate magnetic storm associated with a strong CME and characterized by a very long recovery phase was studied. ENA observations made from the vantage points of

two spacecraft above the northern and southern geohemispheres were utilized to obtain global views of plasma circulation in the inner magnetosphere during this rather minor, but prolonged, magnetic storm event which was characterized by largely northward IMF. The evolution from an initially strongly asymmetric ring current to a more symmetric one was in this way monitored in ENAs.

[73] Modeling of dynamic parameters that represent various current systems showed that the Birkeland Current was the largest contributor during the impulsive start of the storm. Thereafter the symmetric ring current provided the largest contribution.

[74] Magnetic field modeling showed good correspondence with observed ENA symmetries/asymmetries. The moderate but extended response of the geomagnetosphere to the strong disturbance is explained by a long-duration evolution in the orientation of Bz under conditions of enhanced plasma sheet density.

Appendix A: Procedure Adopted for Cleaning NUADU Data

[75] The procedure adopted to clean NUADU data in preparation for analysis is as follows:

[76] 1. The custom developed software integrates 6 frames to form an ENA image.

[77] 2. This software also replaces the Sun pulse pollution unexpectedly found post launch (25 July, 2004) to be present in detector 9 [at azimuth pixel numbers 66–74 (Channel 1); 67–73 (Channel 2); 68–72 (Channel 3)] with estimated mean values.

[78] 3. The convention is adopted that a count recorded by a detector with index “i” (i = 1 to 16) is indicated by C, where also ME = mean and MI = minimum values, then taking mean counts = CME(i) and minimum counts = CMI(i) for each detector, the mean of CMI(i) can be written as:

$$AV_{\min} = \sum CMI(i)/13 \tag{A1}$$

[79] It is noted that measurements from detectors 6, 7 and 11 which progressively became noisy during the mission were not included in this average.

[80] 4. To balance the noise background

$$\mathrm{C}^*(i,j) = \mathrm{C}(\mathrm{i},\mathrm{j}) - \mathrm{CMI}\,(\mathrm{i}) \tag{A2}$$

is estimated. The sun direction is then shifted to azimuth = 0.

[81] 5. The scan area of each detector FOVi = 2πRh$_i$, depends (Figure 12) on its distance from the spin axis. To correct for a resulting overlap in counts we use

FOV1 = FOV16 = 0.12070,
where R = 1, and h1 = 0.01921 = h16;
FOV2 = FOV15 = 0.35758,
where R = 1, and h2 = 0.05691 = h15;
FOV3 = FOV14 = 0.58063,
where R = 1, and h3 = 0.09241 = h14;
FOV4 = FOV13 = 0.78138,
where R = 1, and h4 = 0.12436 = h13;
FOV5 = FOV12 = 0.95127,
where R = 1, and h5 = 0.15140 = h12;
FOV6 = FOV11 = 1.08825,
where R = 1, and h6 = 0.17302 = h11;
FOV7 = FOV10 = 1.15981,
where R = 1, and h7 = 0.18459 = h10;
FOV8 = FOV9 = 1.22522,
where R = 1, and h8 = 0.19500 = h9.

The overlay modification parameter: P(i) = FOVi/FOV8 is given by:

$$C^{**}(i,j) = C^*(i,j)P(i) \tag{A3}$$

[82] After cleaning, counts attributed to background noise (counts lower than ~1.8% of the ENA maximum) are subtracted out.

Appendix B: Method to Retrieve Ion Distributions From NUADU Data

B1. Simulation Equations

[83] Simulation bins for the ENA source were established through dividing the magnetic L shells (from $L = 2$ to $L = 8$) into segments of equal longitude and latitude using a GSM coordinate system. Each volume element was assigned coordinates described by its L shell longitude φ and latitude θ. The space outside the simulation bins was assumed to constitute an optically thin medium with respect to ENA flux (so that ENAs could reach the detectors along the line of sight without undergoing charge exchange).

[84] The counts in each pixel of an ENA image $C_{\delta,\varepsilon}$ (pixel with elevation δ and azimuth ε) was represented in the simulation system by

$$C_{\delta,\varepsilon} = \int dV \Delta E \Delta T \Delta\Omega A(\delta,\varepsilon)[j_{ionH}\sigma_H(E) + j_{ionO}\sigma_O(E)]n, \tag{B1}$$

where dV is the volume element of the line of sight (LOS) of each pixel; ΔE is the energy range within which neutral atoms were collected; ΔT is the time period during which neutral atoms were detected; $\Delta\Omega$ is the solid angle of the volume element pointing to the δ, ε pixel; $A(\delta, \varepsilon)$ is the response function of a detector at that pixel with elevation δ and azimuth ε; ΔS is the cross section of the volume element perpendicular to the line of sight; j_{ionH} and j_{ionO} are the unknown ion fluxes of hydrogen and oxygen; $\sigma_H(E)$ and $\sigma_O(E)$ are the charge exchange cross sections between energetic hydrogen and oxygen ions and cold exospheric neutral atoms, respectively (an average value for σ at the center of each utilized energy channel is adopted for both species); and n is the exospheric neutral atom density near the Earth. Integration is along the LOS of the instrument.

B2. Response Function of the NUADU Detectors

[85] Figure 3 illustrates the geometry of the NUADU detectors. In this system, the ENA flux is emitted from an Earth based volume element (at longitude φ, magnetic latitude λ, and L) with elevation δ^* and azimuth ε^* pointing to the volume element from the sensor. The simplest response

coefficient of a pixel with normal directions δ and ε at the center of the pixel is given by

$$A_{\varphi,\lambda,L}(\delta,\varepsilon) = e_f(\delta)bh\cos\Delta\delta\cos\Delta\varepsilon, \tag{B2}$$

where $e_f(\delta)$ is the total efficiency factor, $\Delta\delta = |\delta^* - \delta|°$, $\Delta\varepsilon = |\varepsilon^* - \varepsilon|°$, and the detector-response length (h) is

$$\begin{cases} h = 0, & \Delta\varepsilon \geq 2.5° \\ h = 1.0 - 22.8\tan\Delta\varepsilon, & 0° < \Delta\varepsilon < 2.5° \end{cases}. \tag{B3}$$

Also, the detector-response width (b) is given by

$$\begin{cases} b = 0, & \Delta\delta \geq 7.5° \\ b = 3.01 - 22.8\tan\Delta\delta, & 4° < \Delta\delta < 7.5° \\ b = 1.42, & \Delta\delta \leq 4° \end{cases}. \tag{B4}$$

The total efficiency factor $ef(\delta)$ is given (section B7) by $e_f(\delta) = E_f(\delta) + C_{\mathrm{Noise}}/C_{\mathrm{Max}}$ (where $E_f(\delta) = 0.91$ is the mean calibration value).

B3. Empirical Model of the Magnetospheric Ion Flux

[86] The ion flux in the ring current region may be modeled, following *Shen and Liu* [2002], in the following form:

$$j_{ion}(L,\phi,\lambda,E,\alpha) = ej_0(L,\phi)\frac{E}{E_0}\left(1 + \left(\frac{E(L/L_0)^3}{\kappa E_0}\right) \cdot \left[\sin\alpha_{eq} + (1 - \sin\alpha_{eq})(L_0/L)^{0.45}\right]^2\right)^{-\kappa-1}, \tag{B5}$$

where λ is the magnetic latitude, α denotes the pitch angle, E_0 represents the typical energy maximum of a particular ion flux and E represents that of a mixed population. The particles of the plasma sheet source region are deemed (following *Christon et al.* [1991]) to follow a Kappa distribution, where $e = (1 + 1/\kappa)^{1+\kappa} \approx 2.962$ (since these latter authors indicated that the most probable values of (k) lie between 5 and 6, a mean value ($\kappa = 5.5$) is adopted here. Also, on the basis of observational data from the International Sun Earth Explorer (ISEE-1) spacecraft, E_0 is set at 7 keV for protons and 16 keV for oxygen ions [*Shen and Liu*, 2002]. $L_0 = 7.3$ is taken to define the outer boundary of the ion injection region of the ring current. The pitch angle (α) of the particles within the volume element can be expressed in terms of λ and α_{eq} (the equatorial pitch angle) such that

$$\sin\alpha = \frac{\left(1 + 3\sin^2\lambda\right)^{1/4}}{\cos^3\lambda}\sin\alpha_{eq}. \tag{B6}$$

[87] The empirical model of *Shen and Liu* [2002] is adopted because it was initially developed to provide a theoretical foundation for the development of the ENA experiment (NUADU) aboard TC-2 and, thereafter, used to make preparations for ENA observational data analysis. It was deduced that ENA H and O should be easily detected by the instrument in the range 10–80 keV. However, comparisons since the launch of TC-2 between NUADU and HENA data by *McKenna-Lawlor et al.* [2005b] showed that, in space, NUADU predominantly detects protons and when the O-ENA flux is exceptionally strong near the Earth during major storms, the proton flux cannot readily be separated in the data from the oxygen ion flux. Both species are combined in the present theoretical treatment within the inversion equation to reflect the presence of a mixed ion population:

$$\begin{aligned} j^*(L,\varphi,\lambda,E,\alpha)\sigma^*(E) \equiv{} & j_{ionH}(L,\varphi,\lambda,E,\alpha)\sigma_H(E_H) \\ & + j_{ionO}(L,\varphi,\lambda,E,\alpha)\sigma_O(E_O) = ej_0^*(L,\varphi) \\ & \cdot \left\{ j_{H0}\frac{\sigma_H(E_H)E_H}{E_{H0}}\left(1 + \left(\frac{E_H(L/L_0)^3}{\kappa E_{H0}}\right)\right.\right. \\ & \left. \cdot \left[\sin\alpha_{eq} + (1 - \sin\alpha_{eq})(L_0/L)^{0.45}\right]^2\right)^{-\kappa-1}, \\ & + j_{O0}\frac{\sigma_O(E_O)E_O}{E_{O0}}\left(1 + \left(\frac{E_O(L/L_0)^3}{\kappa E_{O0}}\right)\right. \\ & \left.\left. \cdot \left[\sin\alpha_{eq} + (1 - \sin\alpha_{eq})(L_0/L)^{0.45}\right]^2\right)^{-\kappa-1}\right\} \end{aligned} \tag{B7}$$

where $\sigma^*(E)$ is a mixed charge exchange cross section, j_0^* (L, φ) represents the dimensionless unknown part of the ion flux introduced to appropriately modify the distribution, and j_{Ho} and j_{0o} are the initial inputs of ion fluxes for proton and oxygen ions provided by an appropriate empirical model. (During the iterative process, $J_{Ho}(L, \phi)$ and J_{Oo} (L, ϕ) represent step improved ion flux inputs of protons and oxygen ions.)

[88] The maximum ion flux obtained depends on the ratio adopted between H and O. In the particular case of the ring current event of 21–22 January analyzed in the present paper (section 3.3), measurements made aboard the Cluster spacecraft of H and O ion fluxes were taken to provide an appropriate mixing ratio during the process of NUADU data deconvolution (section B6).

B4. Exospheric Density Models

[89] The neutral hydrogen densities provided by Chamberlain's classical exospheric model [*Chamberlain*, 1963] are too low to be applicable in the ring current region. Also, the yearly average hydrogen density model of *Østgaard et al.* [2003] cannot be applied in this regime under conditions of elevated solar activity. If conservation of the radial flux of neutral atoms during a large geomagnetic storm is assumed, the exospheric density [*Rairden et al.*, 1986; *Brandt et al.*, 2002] using an adjusted Chamberlain model is represented by

$$n(r,\varphi,\theta) = 3300\exp\left(17.5e^{-1.5r} - \frac{r}{H(\varphi,\theta)}\right), \tag{B8}$$

where

$$H(\varphi,\theta) = 1.46(1 - 0.3\sin\theta\cos\varphi). \tag{B9}$$

[90] Here, r is the geocentric distance, φ is the local time angle from noon and θ is the polar angle from the z axis in

the GSM coordinate system. The coefficient 0.3 in equation (B9) allows the geotail to be represented as axis-symmetric around the Sun-Earth line. All the numerical coefficients in the above expressions derive from a fit to the Chamberlain model made by *Rairden et al.* [1986] and *Brandt et al.* [2002]. It is noted, however, in this context that our present-day knowledge of the true configuration of the geotail is very limited.

B5. Numerical Quadrature Format

[91] The integral in equation (B1) can be calculated numerically along the line of sight to give

$$C_{\delta,\varepsilon} = \Delta T \Delta E \sum_{j,(or,k)} \Delta\Omega_{i,j,k} \frac{A(\delta,\varepsilon)}{S_{i,j,k}} j^{*}_{i,j,k}(L,\lambda,\varphi,E,\alpha)\sigma^{*} \cdot (E) n(L,\lambda,\varphi)_{i,j,k} \Delta l_{i,j,k}, \tag{B10}$$

where i, j, and k represent the φ, λ, and L coordinates of the volume element and n (λ, ϕ) is taken to be a known atom density distribution which could either be from the empirical model or the preceding iterative solution and $\Delta l_{i.j.k}$ is the grid length along the LOS.

[92] The summation operation via j yields a set of linear algebraic equations which can be written in (matrix) form:

$$(C)_p = (K)_{q\times p} (J^{*}_{0}(L,\varphi))_q, \tag{B11}$$

where K is the coefficient matrix with elements of the quadrature weights computed from equation (B10) and J_o* (L, Φ) is a column matrix with elements j_o*(L, Φ), as defined in equation (B7). In equation (B11) the subscripts to the brackets indicate the dimensions of the matrices (where $p < \delta \times \varepsilon$ and $q \le i \times k$, depend on the number of volume elements and on the number of pixels related to the ENA source generated through charge exchange).

B6. Mixed Ion Population

[93] In the course of significant events, the oxygen ion flux usually enhances so that it typically comes to exceed by ~10% the level of the proton flux [*Lennartsson and Sharp*, 1982; *Mitchell et al.*, 2003]. In the particular case of the January 2005 ring current event, the analysis of which is discussed in section 3.3, in situ ion measurements made by the RAPID particle spectrometer aboard CLUSTER [*Wilken et al.*, 1997] on 22 January 2005 between ~2000 and 2300 UT at E > 27 keV (protons) and E > 90 keV (heavy ions/mostly O) are available (E. Daly, private communication, 2009). On the basis of these measurements the values input to the model when analyzing the data of January 2005 (section 3.3) were set at 4×10^5 and 5.7×10^4 $s^{-1}sr^{-1} cm^{-2}keV^{-1}$ for the proton and oxygen ion fluxes, respectively. Following *Shen and Liu* [2002] and section B3, the charge exchange cross sections were taken to be $\sigma_H = 2 \times 10^{-17}$ cm^2 and $\sigma_O = 8 \times 10^{-16}$ cm^2 [*Smith and Bewtra*, 1987] in the center of Channel 2 (NUADU data).

B7. Constrained Linear Inversion

[94] In a strict sense, equation (B11) can only be solved uniquely if the matrix K is square and at the same time nonsingular. However, these two criteria cannot, in practice, be met simultaneously. Instead then of seeking a direct solution, a least squares method (subject to constraint) may be pursued following *DeMajistre et al.* [2004] such that J_o* is determined through minimizing the quantities:

$$(C - KJ^{*}_{0})^{T} \sigma_{C}^{-2} (C - KJ^{*}_{0}) + \gamma J^{*T}_{0} H J^{*}_{0}, \tag{B12}$$

where σ_C^{-2} is the inverse of the measurement covariance matrix, γ is the constraint strength [*Twomey*, 1977], H is a constraint matrix, and T is a transposed matrix. In the present application, $H = H_0 = I$, is adopted as a first-order constraint matrix in an iterative solution. For NUADU data, σ_C^{-2} is a diagonal matrix whose elements are $1/\sigma_i^2$, where σ_i is the uncertainty corresponding to each pixel. Minimizing equation (B12) yields

$$J^{*}_{0} = \left(K^{T} \sigma_{C}^{-2} K + \gamma H\right)^{-1} K^{T} \sigma_{C}^{-2} C. \tag{B13}$$

[95] The relative error is defined by

$$\overline{E}_R = \sqrt{\frac{(C - KJ^{*}_{0})^{T}(C - KJ^{*}_{0})}{C^{T}C}}. \tag{B14}$$

Different constraint strengths (γ) are tried until a minimum value of the relative error is reached.

[96] It was found in practice that for NUADU data the fidelity of image retrieval could be enhanced if, instead of comparing the inversion results with the measurement covariance (following *DeMajistre et al.* [2004]), the inversion results were compared directly with the measurements. The effect obtained using different constraint strengths was monitored as before using the expression for the relative error provided by B14. Only pixels with measurement counts above the noise level were included in the statistics. The noise background was corrected using the total efficiency factor $e_f(\delta) = E_f(\delta) + C_{Noise}/C_{Max}$ where, from the ground calibration, $E_f(\delta) = 0.91$; an average of counts was measured in detectors 1–8 as noise background (C_{Noise}) when they were oriented opposite to the Earth and (C_{Max}) is the count maximum of the image.

Appendix C: Modeling the Dynamics of the Inner Magnetosphere

[97] A simple, flexible model of the responses of the principal field sources in the inner magnetosphere to external driving was developed by *Tsyganenko and Sitnov* [2005]. Each magnetospheric current system was envisaged to show (1) a response to variations in solar wind pressure, which propagate rapidly via Alfven waves inside the magnetosphere, and (2) responses to slower processes, such as reconnection at the magnetopause and particle losses due to pitch angle diffusion and charge exchange. Empirical modeling of these effects was achieved by including a factor W in the total strength of the field force, the magnitude of which behaves with time according to

$$\delta W/\delta t = S - L, \tag{C1}$$

where S and L represent the relevant source and loss functions, respectively. The source term S represents the feeding rate to a current system due to the solar wind input. This is empirically assumed to be a function of the external driving factors and to have the form

$$S = aN^{\lambda}V^{\beta}B_s^{\gamma}, \tag{C2}$$

where N and V are the solar wind density and speed and B_s is the southward component of the IMF. The coefficient a and the power indices λ, β, and γ are unknown parameters of the driving function. L has a different physical meaning depending on which current system is under consideration. If an approach developed by *Burton et al.* [1975] and *Gonzalez et al.* [1994] and its contained references is taken into account, then L can be assumed to be proportional to the difference between the prevailing value of W and its residual, quiet time, level W_o so that

$$L = r(W - Wo). \tag{C3}$$

[98] This yields a solution

$$W(t) = W_0 + \int_0^t S(\tau)\exp[r(\tau - t)]\,d\tau, \tag{C4}$$

where r is the decay rate and the integration time covers the interval from the beginning of the event ($\tau = 0$) to the current moment ($\tau = t$). Formally, the decay rate r can be considered to be an inverse measure of the relaxation time scale $T = 1/r$ (inertia) of a given field source, irrespective of its physical interpretation.

[99] The external field model used by *Tsyganenko and Sitnov* [2005] (following earlier work by *Tsyganenko* [2002a, 2002b]) can be approximated by a linear combination of eight vectors comprising (1) the Chapman-Ferraro field $\mathrm{B}_{\mathbf{CF}}$ that confines the internal field of the Earth within the magnetopause, (2) the inner tail field $\mathrm{B}_{\mathbf{T1}}$, (3) the outer tail field $\mathrm{B}_{\mathbf{T2}}$, (4) the field $\mathrm{B}_{\mathbf{SRC}}$ of a symmetrical ring current, (5) the field of a partial ring current $\mathrm{B}_{\mathbf{PRC}}$, (6) the field of the Region 1 $\mathrm{B}_{\mathbf{R1}}$ Birkeland current, (7) the field of the Region 2 $\mathrm{B}_{\mathbf{R2}}$ Birkeland current, and (8) a penetration component of the IMF given by an interconnection term $\mathrm{B}_{\mathbf{int}} = \varepsilon\mathbf{B}_{\perp}^{\mathrm{IMF}}$. Each of these vectors in the total model field (with the exception of $\mathrm{B}_{\mathbf{CF}}$) was normalized, separately shielded inside the model magnetopause and multiplied by a scalar coefficient representing the magnitude of each source as a function of the prevailing state of the interplanetary medium and of the previous history of external driving. Thus, the total field of the magnetospheric sources assumed the form

$$\begin{aligned}\mathbf{B}^{(\mathrm{mod})} = {} & \mathbf{B}_{\mathrm{CF}} + t_1\mathbf{B}_{\mathrm{T1}} + t_2\mathbf{B}_{\mathrm{T2}} + s\mathbf{B}_{\mathrm{SRC}} + p\mathbf{B}_{\mathrm{PRC}} + b_1\mathbf{B}_{\mathrm{R1}} \\ & + b_2\mathbf{B}_{\mathrm{R2}} + \varepsilon\mathbf{B}_{\perp}^{\mathrm{IMF}},\end{aligned} \tag{C5}$$

where the confining field B_{CF} is defined by the strength and tilt angle of the Earth's dipole and by the shape and size of the magnetopause boundary. This boundary is a predefined surface fitted to the empirical boundary of *Shue et al.* [1998], and deemed by *Tsyganenko and Sitnov* [2005] to be controlled only by the solar wind ram pressure.

[100] The magnitude coefficients appearing in equation (C5) are represented by

$$\begin{aligned} t_1 &= t_1^{(0)} + t_1^{(1)}W_{t1}\big/\sqrt{1 + (W_{t1}/W_{t1c})^2} + t_1^{(2)}(P_d/P_{d0})^{\alpha 1} \\ t_2 &= t_2^{(0)} + t_2^{(1)}W_{t2}\big/\sqrt{1 + (W_{t2}/W_{t2c})^2} + t_2^{(2)}(P_d/P_{d0})^{\alpha 2} \\ s &= s^{(0)} + s^{(1)}W_s\big/\sqrt{1 + (W_s/W_{sc})^2} \\ p &= p^{(0)} + p^{(1)}W_p\big/\sqrt{1 + (W_p/W_{pc})^2} \\ b_1 &= b_1^{(0)} + b_1^{(1)}W_{b1}\big/\sqrt{1 + (W_{b1}/W_{b1c})^2} \\ b_2 &= b_2^{(0)} + b_2^{(1)}W_{b2}\big/\sqrt{1 + (W_{b2}/W_{b2c})^2} \end{aligned} \quad . \tag{C6}$$

[101] Here the solar wind ram pressure P_d is averaged by its normal quiet time value P_{do} = 2 nPa. The driving variables W_{t1}, W_{t2}, W_s, W_p, W_{b1}, W_{b2}, and their respective saturation levels W_{t1c}, W_{t2c}, W_{sc}, W_{pc}, W_{b1c}, and W_{b2c} are individually discussed in *Tsyganenko and Sitnov*'s [2005] paper. The individual variables are defined by

$$W(t_i) = \frac{r}{12}\sum_{k=1}^{i} S_k \exp\left[\frac{r}{60}(t_k - t_i)\right], \tag{C7}$$

where

$$S_k = \left(\frac{N_k}{5}\right)^{\lambda}\left(\frac{V_k}{400}\right)^{\beta}\left(\frac{B_{sk}}{5}\right)^{\gamma}. \tag{C8}$$

[102] Equation (C7) is an equivalent of the integral in the right-hand side of equation (C4), in which integration is replaced by summation over 5 min intervals from the beginning of a storm at $t = t_1$ to the current moment $t = t_i$. In equation (C7) it is assumed that the decay rate r is measured in h^{-1}; while the time (t) is in minutes (thereby introducing the factors 1/12 and 1/60). Thus, defined variables W enter in the six magnitude coefficients in equation (C6), each one having its own decay rate r and a driving function S with an individual set of power indices λ, β, and γ. The coefficient of proportionality ε between the transverse component $\mathbf{B}_{\perp}^{\mathrm{IMF}}$ of the IMF and the interconnection field $\mathbf{B}_{\mathbf{int}}$ in equation (C5) may be assumed [*Tsyganenko*, 2002b] to be a simple binomial function of the IMF clock angle.

[103] **Acknowledgments.** SMcKL thanks Enterprise Ireland for support during the study. L.L. acknowledges the support of the Chinese National Natural Science Foundation Committee grant 40974100. The work at the Max-Planck-Institut fuer Sonnensystemforschung was supported by the Max-Planck-Gesellschaft zur Foerderung der Wissenschaften and the Bundesministerium fuer Bildung und Forschung (BMBF) under grant 50 OC 0501. K.K. acknowledges support from the grant agency VEGA, project 2/7063/27. All the authors thank the reviewers for their constructive comments and suggestions. Appreciation is expressed to the Editors for permission to use a modified version of Figure 6 from *Du et al.* [2008].

[104] Amitava Bhattacharjee thanks Anna Milillo and another reviewer for their assistance in evaluating this paper.

References

Bastanjyan, N. K., A. A. Chilingarian, V. S. Eganov, and G. G. Karapethian (2007), On the production of highest energy solar protons at 20 January, 2005, *Adv. Space Res.*, *39*(9),1454–1457.

Belov, A. V., E. A. Eroshenko, H. Mavromichalaki, C. Plainaki, and V. G. Yanke (2005), Ground level enhancement of the solar cosmic rays on January 20, 2005, *Conf. Pap. Int. Cosmic Ray Conf. 29th*, *1*, 189–192.

Bieber, J. W., J. Clem, P. Evenson, R. Pyle, M. Duldig, J. Humble, D. Ruffolo, M. Ruziwarodom, and A. Saiz (2005), Largest GLE in half a century: Neutron monitor observations of the January 20, 2005 event, *Conf. Pap. Int. Cosmic Ray Conf. 29th*, *1*, 101–104.

Brandt, P. C., R. DeMajistre, E. C. Roelof, D. G. Mitchell, and S. Mende (2002), IMAGE/HENA: Global ENA imaging of the plasma sheet and ring current during substorms, *J. Geophys. Res.*, *107*(A12), 1454, doi:10.1029/2002JA009307.

Burch, J. L. (2000), IMAGE mission overview, *Space Sci. Rev.*, *91*, 114, doi:10.1023/A:1005245323115.

Burton, R. K., R. L. McPherron, and C. T. Russell (1975), An empirical relationship between interplanetary conditions and Dst, *J. Geophys. Res.*, *80*, 4,204-4,214.

Buzulukova, N. Y., Y. I. Galperin, R. A. Kovrazhkin, A. L. Glazunov, G. A. Vladimirova, H. Stenuit, J. A. Sauvaud, and D. C. Delcourt (2002), Two types of ion spectral gaps in the inner magnetosphere: Interball-2 observations and modeling, *Ann. Geophys.*, *20*, 349-364.

Chamberlain, J. W. (1963), Planetary coronae and atmospheric evaporation, *Planet. Space Sci.*, *11*(8), 901–960, doi:10.1016/0032-0633(63)90122-3.

Christon, S. P., D. J. Williams, and D. G. Mitchell (1991), Spectral characteristics of plasma sheet ion and electron populations during disturbed geomagnetic condition, *J. Geophys. Res.*, *96*, 1–22, doi:10.1029/90JA01633.

Daglis, I. A., R. M. Thorne, W. Baumjohann, and S. Orsini (1999), The terrestrial ring current: Origin, formation, and decay, *Rev. Geophys.*, *37*(4), 407-438.

Dandouras, I., H. Reme, and J. Cao (2008), Energetic ion dynamics of the inner magnetosphere from quiet conditions to extreme solar events, paper S2–5 presented at Third International Symposium on KuaFu Project, Chin. Acad. of Sci., Kunming, China, 14–19 Sept.

Dandouras, I., H. Rème, J. Cao, and P. Escoubet (2009), Magnetosphere response to the 2005 and 2006 extreme solar events as observed by the Cluster and Double Star spacecraft, *Adv. Space Res.*, *43*, 618–623.

D'Andrea, C., and J. Poirier (2005), Ground level muons coincident with the 20 January 2005 solar flare, *Geophys. Res. Lett.*, *32*, L14102, doi:10.1029/2005GL023336.

Davis, T. N., and M. Sugiura (1966), Auroral electrojet activity index AE and its universal time variations, *J. Geophys. Res.*, *71*, 785–801.

DeMajistre, R., E. C. Roelof, P. C. Brandt, and D. G. Mitchell (2004), Retrieval of global magnetospheric ion distributions from high energy neutral atom (ENA) measurements made by the IMAGE/HENA instrument, *J. Geophys. Res.*, *109*, A04214, doi:10.1029/2003JA010322.

Domingo, V., B. Fleck, and A. I. Poland (1995), The SOHO mission: An overview, *Sol. Phys.*, *162*, 1–37, doi:10.1007/BF00733425.

Du, A. M., R. T. Tsurutani, and W. Sun (2008), Anomalous geomagnetic storm of 21–22 January 2005: A storm main phase during northward IMFs, *J. Geophys. Res.*, *113*, A10214, doi:10.1029/2008JA013284.

Flückiger, E. O., R. Bütikofer, M. R. Moser, and L. Desorgher (2005), The cosmic ray ground level enhancement during the Forbush decrease in January 2005, *Conf. Pap. Int. Cosmic Ray Conf. 29th*, *1*, 225–228.

Foullon, C., C. J. Owen, S. Dasso, L. M. Green, I. Dandouras, H. A. Elliott, A. N. Fazakerly, Y. V. Bogadnova, and N. U. Crooker (2007), Multi-spacecraft study of the 21 January 2005 ICME: Evidence of current sheet substructure near the periphery of a strongly expanding, fast magnetic cloud, *Sol. Phys.*, *244*, 139–165, doi:10.1007/s11207-007-0355-y.

Fränz, M., and D. Harper (2002), Heliospheric coordinate systems, *Planet. Space Sci.*, *50*(2), 217–233, doi:10.1016/S0032-0633(01)00119-2.

Gonzalez, W. D., J. A. Joselyn, Y. Kamide, H. W. Kroehl, G. Rostoker, B. T. Tsurutani, and V. M. Vasyliunas (1994), What is a geomagnetic storm? *J. Geophys. Res.*, *99*(A4), 5771–5792, doi:10.1029/93JA02867.

Greenspan, M. E., and D. C. Hamilton (2000), A test of the Dessler-Parker-Sckopke relation during magnetic storms, *J. Geophys. Res.*, *105*, 5419–5430.

Hamilton, D. C., G. Gloeckler, F. M. Ipavich, W. Studemann, B. Wilken, and G. Kremser (1988), Ring current development during the great geomagnetic storm on February 1986, *J. Geophys. Res.*, *93*, 14,343–14,355, doi:10.1029/JA093iA12p14343.

Kalegaev, V. V. (2006), Magnetospheric state during the 20 January, 2005 GLE, paper presented at Eighth Management Committee Meeting (MCM) and Workshop of COST, Eur. Coop. in Sci. and Technol., Antalya, Turkey, 27–30 March.

Kalegaev, V. V., N. Y. Ganushkina, T. I. Pulkkinen, M. V. Kubyshkina, H. J. Singer, and C. T. Russell (2005), Relation between the ring current and the tail current during magnetic storms, *Ann. Geophys.*, *23*, 523–533.

Krucker, S., G. J. Hurford, and R. P. Lin (2005), RHESSI X-ray and Gamma-ray observations of the January 20 2005 event, *Eos Trans. AGU*, *86*(52), Fall Meet. Suppl., Abstract SH 21A- 01.

Kudela, K., R. Bučík, and P. Bobík (2008), On transmissivity of low energy cosmic rays in disturbed magnetosphere, *Adv. Space Res.*, *42*, 1300–1306.

Kuznetsov, V. V., G. Kurt, B. Y. Yushkov, I. N. Myagkova, K. Kudela, K. Kassovicova, and M. Slivka (2005), Proton acceleration during 20 January 2005 solar flare: CORONAS-F observations of high-energy gamma emission and GLE, *Conf. Pap. Int. Cosmic Ray Conf. 29th*, *1*, 49–52.

Kuznetsov, S. N., V. G. Kurt, B. Y. Yushkov, I. N. Myagkova, K. Kudela, J. Kaššovicová, and M. Slivka (2006a), Proton acceleration during 20 January 2005 solar flare: CORONAS-F observations of high-energy γ emission and GLE, *Contrib. Astron. Obs. Skalnate Pleso*, *36*(2), 85–92.

Kuznetsov, S. N., B. Y. Yushkov, J. Kaššovicová, K. Kudela, and R. Bucik (2006b), Changes of geomagnetic transmissivity in the disturbed magnetosphere: Ground based and CORONAS-F observations, *Czech. J. Phys.*, *56*, 629–639, doi:10.1007/s10582-006-0171-x.

Lennartsson, W., and R. D. Sharp (1982), A comparison of 0.1–17 keV/e ion composition in the near equatorial magnetosphere between quiet and disturbed conditions, *J. Geophys. Res.*, *87*, 6109–6120.

Liu, Z. X., C. P. Escoubet, Z. Pu, H. Laakso, J. K. Shi, C. Shen, and M. Hapgood (2005), The Double Star Mission, *Ann. Geophys.*, *23*, 2707–2712.

Lu, L., et al. (2008), Iterative inversion of global magnetospheric ion distributions using energetic neutral atom (ENA) images recorded by the NUADU/TC-2 instrument, *Ann. Geophys.*, *26*, 1641–1652.

Lyons, L. R., and M. Schulz (1989), Access of energetic particles to storm time ring current through enhanced radial diffusion, *J. Geophys. Res.*, *94*, 5491–5496, doi:10.1029/JA094iA05p05491.

McKenna-Lawlor, S., et al. (2004), The energetic NeUtral Atom Detector Unit (NUADU) for China's Double Star Mission and its calibration, *Nucl. Instrum. Methods Phys. Res., Sect. A*, *530*, 311–322.

McKenna-Lawlor, S., et al. (2005a), An overview of the scientific objectives and technical configuration of the Neutral Atom Detector Unit NUADU on the Chinese Double Star Mission, *Planet. Space Sci.*, *53*(1–3), 335–348, doi:10.1016/j.pss.2004.09.060.

McKenna-Lawlor, S., et al. (2005b), The NUADU experiment on TC-2 and the first Energetic Neutral Atom (ENA) images recorded by this instrument, *Ann. Geophys.*, *23*, 2825–2849.

Mewaldt, R. A., M. D. Looper, C. M. S. Cohen, G. M. Mason, D. K. Haggerty, M. I. Desai, A. W. Labrador, R. A. Leske, and J. E. Mazur (2005), Solar particle energy spectra during the large events of October–November, 2003 and January, 2005, *Conf. Pap. Int. Cosmic Ray Conf. 29th*, *1*, 101–104.

Mitchell, D. G., H. D. Voss, D. Prentice, K. C. Hsieh, C. C. Curtis, and F. R. Powell (2000), High energy neutral atom HENA imager for the IMAGE mission, *Space Sci. Rev.*, *91*, 67–112, doi:10.1023/A:1005207308094.

Mitchell, D. G., P. C:son Brandt, E. C. Roelof, D. C. Hamilton, K. C. Retterer, and S. Mende (2003), Global imaging of O+ from IMAGE/HENA, *Space Sci. Rev.*, *109*, 63–75, doi:10.1023/B:SPAC.0000007513.55076.00.

Miyasaka, H., et al. (2005), The Solar Event on 20 January 2005 observed with the Tibet YBJ Neutron monitor observatory, *Conf. Pap. Int. Cosmic Ray Conf. 29th*, *1*, 241–244.

Østgaard, N., S. B. Mende, H. U. Frey, G. R. Gladstone, and H. Lauche (2003), Neutral hydrogen density profiles derived from geocoronal imaging, *J. Geophys. Res.*, *108*(A7), 1300, doi:10.1029/2002JA009749.

Paxton, L. J., J. Kozyra, B. DeMagjistre, H. Kil, D. Morrison, B. Wolven, D. Mitchell, P. Brandt, Y. Zhang, and C. Meng (2005), Observations of solar and magnetospheric inputs and atmospheric responses to the January 2005 long duration flares and fast coronal mass ejections, *Eos Trans. AGU*, *86*(18), Jt. Assem. Suppl., Abstract SA41A–06.

Perez, J. D., M.-C. Fok, and T. E. Moore (2000), Deconvolution of energetic neutral atom images of the Earth's magnetosphere, *Space Sci. Rev.*, *91*, 421–436, doi:10.1023/A:1005277307611.

Perez, J. D., G. Kozlowski, P. C. Brandt, D. G. Mitchell, J. M. Jahn, C. J. Pollock, and X. Zhang (2001), Initial ion equatorial pitch angle distributions from energetic neutral atom images obtained by IMAGE, *Geophys. Res. Lett.*, *28*, 1155–1158.

Rairden, R. L., L. A. Frank, and J. D. Craven (1986), Geocoronal imaging with dynamics explorer, *J. Geophys. Res.*, *91*, 13,613–13,630, doi:10.1029/JA091iA12p13613.

Reme, H., et al. (2005), The HIA instrument on board the Tan-Ce 1 Double Star near-equatorial spacecraft, *Ann. Geophys.*, *23*, 2757–2774.

Roelof, E. C. (1987), Energetic neutral atom image of a storm time ring current, *Geophys. Res. Lett.*, *14*, 652–655, doi:10.1029/GL014i006p00652.

Roelof, E. C., and A. J. Skinner (2000), Extraction of ion distributions from magnetospheric ENA and EUV images, *Adv. Space Res.*, *91*, 437–459.

Ryan, J. M., et al. (2005), Ground level events measured with Milagro, *Conf. Pap. Int. Cosmic Ray Conf. 29th*, *1*, 245–248.

Share, G. H., R. J. Murphy, D. M. Smith, A. Y. Shih, G. J. Hurford, R. R. A. Schwarz, A. J. Tylka, and R. P. Lin (2006), RHESSI spectroscopic observations of the 2005 January 20 solar flare, paper presented at 37th Meeting of the AAS Solar Physics Division, Durham, N. H., 25–30 June.

Shen, C., and Z. X. Liu (2002), Properties of the neutral energetic atoms emitted from Earth's ring current region, *Phys. Plasmas*, *9*, 3984–3994.

Shue, J.-H., et al. (1998), Magnetopause location under extreme solar wind conditions, *J. Geophys. Res.*, *103*, 17,691–17,700, doi:10.1029/98JA01103.

Smith, P. H., and N. K. Bewtra (1987), Charge exchange lifetimes for ring current ions, *Space Sci. Rev.*, *22*, 301–318.

Stone, E. C., A. M. Frandsen, R. A. Mewaldt, E. R. Christian, D. Margolies, J. F. Ormes, and F. Snow (1998), The Advanced Composition Explorer, *Space Sci. Rev.*, *86*, 1–22, doi:10.1023/A:1005082526237.

Thomsen, M. F., J. E. Borovsky, D. J. McComas, and M. R. Collier (1998), Variability of the ring current source population, *Geophys. Res. Lett.*, *25*, 3481–3484.

Tsyganenko, N. A. (2002a), A model of the near magnetosphere with a dawn-dusk asymmetry: 1. Mathematical structure, *J. Geophys. Res.*, *107*(A8), 1179, doi:10.1029/2001JA000219.

Tsyganenko, N. A. (2002b), A model of the near magnetosphere with a dawn-dusk asymmetry: 2. Parameterization and fitting to observations, *J. Geophys. Res.*, *107*(A7), 1176, doi:10.1029/2001JA000220.

Tsyganenko, N. A., and M. I. Sitnov (2005), Modeling the dynamics of the inner magnetosphere during strong geomagnetic storms, *J. Geophys. Res.*, *110*, A03208, doi:10.1029/2004JA010798.

Twomey, S. (1977), Introduction to the mathematics in remote sensing and indirect measurements, *Dev. Geomath.*, vol. 3, Elsevier Sci., New York.

Vallat, C., et al. (2004), First comparisons of local ion measurements in the inner magnetosphere with ENA magnetospheric image inversions: Cluster-CIS and IMAGE-HENA observations, *J. Geophys. Res.*, *109*, A04213, doi:10.1029/2003JA010224.

Vallat, C., I. Dandouras, P. Escoubet, H. Reme, J. Cao, A. Balogh, and C. Carr (2005), Magnetospheric response to extreme solar events of January 2005, as observed by the Cluster and Double Star spacecraft, *Eos Trans. AGU*, *86*(18), Jt. Assem. Suppl., Abstract SM51A–03.

Vallat, C., N. Ganushkina, I. Dandouras, C. P. Escoubet, M. G. G. T. Taylor, H. Laakso, A. Masson, J.-A. Sauvaud, H. Rème, and P. Daly (2007), Ion multi-nose structures observed by Cluster in the inner magnetosphere, *Ann. Geophys.*, *25*, 171–190.

Wanliss, J. A., and K. M. Showalter (2006), High-resolution global storm index: Dst versus SYM-H, *J. Geophys. Res.*, *111*, A02202, doi:10.1029/2005JA011034.

Wilken, B., et al. (1997), RAPID: The imaging energetic particle spectrometer on Cluster, *Space Sci. Rev.*, *79*, 399–473, doi:10.1023/A:1004994202296.

Yanke, V. G., L. M. Baisultanova, A. V. Belov, R. Butikofer, E. A. Eroshenko, E. O. Fluckiger, G. Mariatos, and H. Mavromichalaki (2005), Variations of geomagnetic cutoff rigidities during the series of geomagnetic storms in January 2005: Observations and modeling, *Conf. Pap. Int. Cosmic Ray Conf. 29th*, *1*, 101–104.

J. Balaz, S. McKenna-Lawlor, and I. Strharsky, Space Technology Ireland, National University of Ireland, Maynooth, Maynooth Co. Kildare, Ireland. (stil@nuim.ie)

S. Barabash, Swedish Institute of Space Physics, SE-981 28 Kiruna, Sweden.

P. C. Brandt and Y. Zheng, Johns Hopkins University Applied Physics Laboratory, Laurel, MD 20723, USA.

R. Bucik, Max Planck Institute for Solar System Research, D-37191 Lindau, Germany.

I. Dandouras, Centre d'Etude Spatiale des Rayonnements, Université de Toulouse, and UMR 5187, CNRS, F-31028 Toulouse, France.

K. Kudela, Institute of Experimental Physics, 040 01 Kosice, Slovakia.

L. Li, Center for Space Science and Applied Research of the Chinese Academy of Sciences, Beijing 8701, China.